Simulation of ECN Diesel Spray A Using Conditional Source-term Estimation

Xiao Hang Fang[a,*], Riyaz Ismail[a,*], Kendal Bushe[b] and Martin Davy[a]

[*]The authors contribute equally to this paper; [a]Department of Engineering Science, University of Oxford, UK OX1 3PJ; [b]Department of Mechanical Engineering, The University of British Columbia, Vancouver, BC, Canada V6T 1Z4;

ARTICLE HISTORY
Compiled June 8, 2020

ABSTRACT
A novel combustion modelling approach is proposed here to study the transient effects of diesel spray. Conditional Source-term Estimation (CSE) is a combustion model which invokes the Conditional Moment Closure (CMC) hypothesis to provide an approximation of the mean chemical source term in an averaged transport equation. Unlike CMC, where transport equations are solved for conditional moments, CSE recovers these conditional moments through the solution of an inverse problem. Integral equations are inverted for the conditional moments, by assuming spatial homogeneity in the conditional averages where Tikhonov regularization is applied. Previous CSE studies have shown that the model is able to predict the flame characteristics successfully for both premixed and non-premixed combustion modes. However, most of these investigations were based on methane flames. This study will be the first successful application of CSE to a complex hydrocarbon fuel, n-dodecane, under the Engine Combustion Network's (ECN) "Spray A" conditions. Detailed chemistry is included in tabulated form using the Flamelet Generated Manifold (FGM) methodology. The predictions of this study include both the Favre averaged conditional mass fraction of reactive species and temperature. The results are compared with available experimental data and previous numerical results. Both RANS and LES simulations are performed under the same condition. The objectives of the paper are (i) assessment of the application of CSE on igniting diesel spray (ii) comparison of the CSE numerical results with available experimental results and previous numerical simulations. Overall, the combination of a chemical mechanism that has been tuned to predict "Spray A" conditions with the CSE-FGM model is able to successfully predict autoignition delay time and lift-off length of n-dodecane spray within the scatter of the experimental data. CSE-FGM offers a feasible tool for detailed combustion analysis of diesel spray flames. Both RANS and LES can give reasonably good global predictions of the flame.

KEYWORDS
Conditional Source-Term Estimation; turbulent non-premixed combustion; Spray A; n-dodecane; Ignition; CFD

1. Introduction

Reacting spray modelling remains one of the biggest challenges in combustion modelling. However, the broad usage of liquid fuel in practical applications such as industrial burners, aero-engines and IC engines makes reacting spray modelling critical to

[*]Corresponding Author. Email: xiaohang.fang@eng.ox.ac.uk

represent thermodynamic properties in these systems accurately. Diesel sprays, an essential element of compression ignition engine operation, are typically characterized as a non-premixed liquid fuel injection process. The combustion process is primarily seen as mixing-controlled non-premixed combustion. Apart from the dedicated stochastic partial differential function (PDF) approach, there are three common approaches for non-premixed combustion: the infinitely fast chemistry model (FCM) approach, the laminar flamelet model (LFM) approach and the Conditional Moment Closure (CMC) approach.

With the FCM, the mean reaction rate $\bar{\dot{\omega}}_k$ is assumed to be correlated with a conserved scalar in the whole flow through a deterministic function $\bar{\dot{\omega}}_k = \bar{\dot{\omega}}_k(\eta)$. η is the sample space for the conditioning variable, which, for non-premixed combustion is typically chosen to be the mixture fraction (which, as a random variable, would have the symbol Z). Using the infinitely FCM hypothesis might be acceptable when reactions in a system are close to their equilibrium state, for example; in homogeneous charge compression ignition (HCCI) and premixed charge compression ignition (PCCI) systems. However, it is inadequate to describe a conventional diesel combustion system where non-equilibrium, transient and non-homogeneous reaction processes are present throughout the flow field. To account for finite chemistry effects in turbulent combustion modelling, both LFM approaches and CMC approaches were developed. Through the transformation of physical coordinates, both approaches solve the diffusion-reaction process in mixture fraction space [1].

The LFM approach decouples a three-dimensional flame structure into an ensemble of one-dimensional microscopic flame elements called flamelets. Flamelet models have been successfully used in both Large Eddy Simulations (LES) and Reynolds-average Navier-Stokes (RANS) simulations of turbulent reacting flows. Studies have used both premixed and non-premixed generated manifolds [2][3], along with unsteady diffusion flamelets [4]. Although these methods have been successfully applied to different turbulent flames, it has been found that most LFM models are inadequate to simulate flows with a practically wide range of time-scales. Challenges were encountered, especially when LFM models were used to address multiple combustion regimes (premixed, partially premixed and diffusion flames) in a single system.

Established independently by Klimenko [5] and Bilger [6], CMC is based on the fact that fluctuations in scalar quantities can be significantly reduced after conditioning with one principle quantity. Mixture fraction, Z, is used as a conditioning variable for non-premixed combustion because experiments have shown that mixture fraction plays an integral role in determining quantities such as mean reaction rates and temperature [7][8]. Unlike flamelet models, the CMC model has less constraint regarding flame regime, which in principle allows it to accommodate all practical cases. Solutions of CMC equations will provide conditional temperature and mass fractions of all species at all locations and time in the flow field. CMC has been a great success in a wide variety of non-premixed combustion problems including turbulent lifted flames [9], autoigniting methane [10] and turbulent pilot flames [11]. CMC has also been found suitable for both soot formation predictions in turbulent non-premixed methane jet flames [12] and two-phase flows [13].

In terms of diesel spray studies, CMC has successfully captured spray evolution, ignition delay and pressure development in a closed combustion chamber at diesel engine conditions [14]. Good agreement between computational results and experimental results were observed for n-heptane spray autoignition characteristics using CMC under diesel engine conditions [15]. More recently, Blomberg *et al.* [16] investigated n-dodecane split injections of "Spray A" using CMC combustion model with

both RANS and LES turbulence treatments. LES-CMC was able to capture transient phenomena (combustion recession) after the end of the first injection, whereas RAN-CMC was not successful in obtaining all combustion recession details. Among all these models, the first-order conditional moment hypothesis is used. However, when extinction and reignition phenomena are present, first conditional moment closure in CMC will break down. One refinement is to use higher-order closure which is also derived in Bilger and Klimenko's joint paper [17]. Han and Huh [18] used both first and second-order Lagrangian CMC methods to study piloted jet diffusion flames near extinction. The second-order CMC model showed a noticeable improvement of species mass fraction compared to the first-order CMC model. Kim *et al.* [19] applied a second-order CMC model to a turbulent non-premixed hydrocarbon flame where significant local extinction and reignition are present. The model has shown improvements in predicting intermediate species; however, additional modelling is required for unclosed terms which makes it less appealing. Another approach is to introduce a second conditioning variable in conjunction with the mixture fraction. Pitsch *et al.* [20] introduced scalar dissipation rate as the variable due to its physical significance in extinction/reignition phenomena [21]. The method describes extinction in the flame reasonably well; however, the onset reignition prediction is too early.

More recently, Kronenberg [22] adopted sensible enthalpy as a second conditioning variable and presented excellent computational results in agreement with DNS results at all times. The success of capturing extinction and reignition makes CMC an excellent candidate for modelling combustion systems covering different regimes however CMC models are still computationally expensive not only due to the modelling of unclosed terms in transport equations, but also the additional dimension in CMC equations introduced by the conditioning variable. Therefore it is of our interests to find another combustion model that inherits CMC's advantage of having fewer constraints on combustion regimes but requires less computational resources when higher-order closure or a second conditioning variable is introduced. First proposed by Bushe and Steiner [23], Conditional Source-term Estimation (CSE) is a combustion model which invokes the CMC hypothesis. A more detailed model description will be included in Section 2. Previous CSE studies have shown that the model can predict the flame characteristics successfully for both premixed and non-premixed combustion modes [24] [25]. The inclusion of a second conditioning variable also successfully enabled CSE to simulate partially premixed lifted jet flames accurately [26]. However, most of these investigations were based on methane flames. Therefore the extension of the combustion model to complex hydrocarbon fuels is attractive and worth investigating.

This work provides an assessment of the performance of the novel Conditional Source-term Estimation with Flamelet Generated Manifold (CSE-FGM) combustion model in the diesel spray context. The objectives of the paper are (i) assessment of the application of CSE to igniting diesel spray (ii) comparison of the CSE numerical results with available experimental results and previous numerical simulations. An assessment of the new CSE approach is presented comparing the measured experimental data taken from the engine combustion network (ECN). In particular, ignition delay, lift-off and flame location are discussed. The main differences of the predicted flame structure described by the representative species and temperature distribution are elaborated in detail.

2. Numerical Methodology

The CFD solver used in present work is CONVERGE, together with user-defined models developed by the authors to simulate engine relevant reacting sprays. CONVERGE is a general-purpose CFD code for computing three dimensional chemically reacting fluid flows. The gas phase in this study is described using both the RANS and LES formulations, and the conservation equations are solved for a compressible multi-component flow using a finite volume, second-order accurate discretization method. Pressure and velocity coupling are achieved using the well-known PISO algorithm. The turbulence is modelled using standard $k-\epsilon$ model with modified constants. A variable time step is employed with each time-step following the Courant-Friedrichs-Lewy (CFL) criteria. The maximum convective and diffusive CFL applied in this study is 1 and 2, respectively. The spray is modelled in a Eulerian-Lagrangian fashion where parcels are tracked in the CFD domain while exchanging mass, momentum and energy with the gas phase. Different spray sub-models are employed to describe liquid atomization, break up, collision, evaporation and heat transfer. As mentioned earlier, in order to validate the CSE-FGM approach, the results will also be compared with the experimental and previous simulation studies. In the following sections, first, a brief overview of the chosen spray sub-models is given, and then details of two combustion models are presented with a focus on the newly developed CSE-FGM model.

2.1. Liquid spray sub-models

A conventional "Blob" injection model is employed to simulate the spray injection process where"parcels" are injected into the computational domain with the same characteristic size as the nozzle diameter. Droplet break-up and atomization are modelled using the Kelvin-Helmholtz Rayleigh-Taylor (KH-RT) model. The activation of KH or RT is correlated to a break-up length L_b defined as:

$$L_b = C_{bl}\sqrt{\frac{\rho_l}{\rho_g}}d_0 \tag{1}$$

where C_{bl} is the break-up length constant. The region inside the characteristic break-up length is only computed using KH accounting for the break-up of large drops due to surface wave growth, causing instabilities. When beyond the break-up length, both KH and RT are employed. KH will be used to first form child droplets, where RT will account for child droplet break-up caused by the rapid deceleration of the droplets from aerodynamic drag. The droplet break-up rate is calculated using:

$$\frac{dr_p}{dt} = -\frac{r_p - r_c}{\tau} \tag{2}$$

with parent droplet radius (r_p), child droplet radius (r_c) and break-up timescale (τ). The inherent grid sensitivity of the KH-RT model has been studied previously for the non-reacting "Spray A" conditions and validated against another commercial CFD solver [27]. Droplet collision is described using the No Time Counter (NTC) model and the droplet drag is accounted for using the dynamic drag model. The evaporation process is modelled using the Frossling correlation. The effects of turbulence on droplets are characterized using the stochastic dispersion model, where turbulence is modelled using the standard $k-\epsilon$ model with modified constants. Detailed model

constants and boundary conditions can be found in our previous studies [28]. A list of chosen sub-models is presented in Table: 1.

Table 1. Modeling Setup for Non-reacting Simulations

Model Setup	**Selected Model**
Spray Models	
Injection models	Blob
Atomization and Break up	KH-RT
Collision	NTC
Drag	Dynamic
Evaporation	Frossling
Dispersion	Stochastic
Heat Transfer	Ranz-Marshall
Grid	
Type	Structured with AMR
Dimensionality	3D
Time Step	Variable Time Step

2.2. Conditional Source-term Estimation (CSE)

For simulations that are not fully resolved i.e. RANS and LES, obtaining filtered or averaged reaction rates directly from filtered or averaged values of the scalar field leads to unacceptable discrepancies compared to fully resolved results. CSE seeks closure of the chemical source term using the same first order conditional moment closure hypothesis as in CMC. However, instead of solving transport equations for conditionally averaged scalars, CSE estimated conditional means from unconditionally averaged scalars. Similar to CMC, the mean conditional chemical source term for species k is written as:

$$\overline{\dot{\omega}_k|\eta} \approx \dot{\omega}_k(\overline{T|\eta}, \overline{Y_k|\eta}, \overline{\rho|\eta}) \tag{3}$$

where η is the discretised conditioning variable, which, for non-premixed combustion, is chosen to be mixture fraction; $\overline{T|\eta}$, $\overline{Y_k|\eta}$ and $\overline{\rho|\eta}$ are the conditionally averaged temperature, mass fraction of species k and density respectively. The unconditionally averaged chemical source term is therefore:

$$\bar{\dot{\omega}}_k(\vec{x}, t) = \int_0^1 \overline{\dot{\omega}_k|\eta}(\eta, \vec{x}, t)\bar{P}(\eta, \vec{x}, t)d\eta \tag{4}$$

In this equation, $\bar{P}(\eta, \vec{x}, t)$, is the Favre averaged PDF of mixture fraction, usually assumed to be a β-function [29]. Similarly the unconditionally averaged scalar at any spatial location $\vec{x}$ and time t, such as Favre averaged species mass fraction $\bar{Y}_k$ can be expressed as

$$\bar{Y}_k(\vec{x}, t) = \int_0^1 \overline{Y_k|\eta}(\eta, \vec{x}, t)\bar{P}(\eta, \vec{x}, t)d\eta \tag{5}$$

The conditionally averaged scalars are then computed through inversion of Equation 5. At this point it is necessary to discuss properties and tools that can simplify the inversion process. DNS and experimental studies have shown conditional averages vary much less in space than unconditional averages, therefore it is reasonable to assume some spatial homogeneity of the conditional means for many flows [23]. With this assumption a group of localised cells, referred to as an ensemble, may be selected in the flow field with statistical homogeneity in conditional averages:

$$\overline{Y_k|\eta}(\eta, \vec{x}, t) \approx \left\langle \overline{Y_k|\eta} \right\rangle_A \qquad x \in A \tag{6}$$

where $\left\langle \overline{Y_k}|\eta \right\rangle_A$ is the ensemble conditional average of species k mass fraction. Equation 5 can then be rewritten as:

$$\bar{Y}_k(\vec{x}, t) \approx \int_0^1 \left\langle \overline{Y_k|\eta} \right\rangle_A \bar{P}(\eta, \vec{x}, t) d\eta \tag{7}$$

In practice, how these ensembles are defined ultimately depends on the particular flow being simulated. In jet geometries, ensembles are typically divided along the axial direction, taking advantage of weak radial dependence of conditional averages in jets [30]. In order to produce an independent solution, while minimizing the computational cost, the number of ensembles is best determined through a sensitivity analysis [24]. To compute conditional averages, Equation 7 can be treated as a Fredholm equation of the first kind with $\bar{P}(\eta, \vec{x}, t)$ as the kernel [31]. The equation can be rewritten as:

$$\vec{b} = \mathbf{A}\vec{\alpha} \tag{8}$$

where $\vec{b}$ is the unconditional Favre mean mass fraction of species k at $\vec{x}$ position; $\mathbf{A}$ is an $N \times M$ matrix of the integrated PDF over some interval of the mixture fraction; N is the number of points in each ensemble and M is the number of discrete bins in mixture fraction space; α stands for the conditional mean in the $\mathrm{M}_t h$ mixture fraction bin. The number of points in each ensemble is limited to 10,000 [32] where the number of discrete bins for mixture fraction are chosen as 50 [31] based on previous studies for methane-air cases. In matrix notation, $\mathbf{A}$ can be computed using:

$$A_{jm} = \int_{\eta 1}^{\eta 2} \bar{P}(\eta_m, \vec{x}, t) d\eta \tag{9}$$

The direct solution of Equation 8, $\vec{\alpha} = \mathbf{A}^{-1}\vec{b}$, is sensitive to any perturbations in the system which makes it an ill-posed problem [33]. There are several ways of addressing this issue; Bushe and Steiner [23] proposed to minimize the residual of Equation 7 and the conditional averages' derivatives with respect to mixture fractions. A more common method, *Tikhonov Regularisation*, was later introduced by Grout *et al.* [25]. This regularization method is based on *a priori* knowledge of the solution, and can be applied to Equation 8 by reformulating it into a minimization problem (a least-square problem):

$$\vec{\alpha} = argmin \left\| \begin{bmatrix} A \\ \lambda I \end{bmatrix} \vec{\alpha} - \begin{bmatrix} \vec{b} \\ \lambda \vec{\alpha}^0 \end{bmatrix} \right\|_2^2, \tag{10}$$

where notation $\|\cdot\|_2$ is the L2 norm of a vector, I is the identity matrix, λ is the regularization parameter, which is evaluated based on the characteristics of the inversion problem, and $\vec{\alpha}^0$ is the prior knowledge of solution which may take any initial value as the solution will be independent of this. Values close to the final solution of $\vec{\alpha}$ can provide a faster convergence which could significantly reduce the computational cost. An option for a prior solution would be using solutions from the previous time-step. The regularization parameter is set to [25]:

$$\lambda = \frac{Tr(A^T A)}{I} \tag{11}$$

where Tr is the trace of the matrix. In this study, the regularization solution is set to be the laminar flamelet solution. Finally, LU decomposition can be applied to solve Equation 8.

CSE is more computationally efficient compared to CMC owing to this inversion process. It also possesses the advantage of CMC that no assumptions are made regarding flame regimes. Similar to CMC, doubly Conditional Source-term Estimation (DCSE) can also be used to predict combustion instabilities such as reignition and extinction. Dovizio *et al.* [26],[34] studied both turbulent stratified V-shaped flames and a series of lifter turbulent jet flames using DCSE. The local ignition/extinction phenomenon was successfully captured in both cases. Apart from all the advantages of CSE, directly including detailed chemistry in CSE is still challenging; especially with hydrocarbon fuels, which involve hundreds of species and reactions. Inverting each species in these fuels would be computationally prohibitive, and species transport equations will be too stiff for any current ODE solvers to handle. Therefore a reduced chemistry model of some sort is necessary so that a limited number of scalars can represent the detailed chemistry. A further challenge arises when trying to combine CSE with full chemistry - or even skeletal chemistry: when one inverts for conditional averages of species mass fractions, there is inevitably an error in the result, however slight. If one inverts for every species mass fraction independently, there is no way to ensure elemental mass conservation, which is almost certain to lead to unphysical reaction rates when those conditional averages are substituted into the reaction rate expressions. Thus, it is necessary to invert integral equations for all species simultaneously, imposing elemental mass conservation as a constraint on the solution; for full chemistry - even for only methane - this would be prohibitively expensive; it is still likely to be very expensive with even a highly-reduced skeletal mechanism. This suggests those past simulations using CSE that used a low-dimensional manifold representation of chemistry was successful because they used a manifold (where elemental mass conservation is guaranteed) - that is to say, the use of the manifold was intrinsic to the success of the method, rather than merely a convenient and inexpensive representation of the chemistry. The entire solving process is depicted in Figure 1, which includes interactions of each component in CSE.

3. Tabulated Chemistry Approach

In a low-dimensional manifold approach, chemical source terms are tabulated prior to the simulation to save computational time. Different approaches have been used before to incorporate reduced chemistry into CSE before for the speed and the accuracy of the calculation. When first implemented, Bushe and Steiner used a single-step chem-

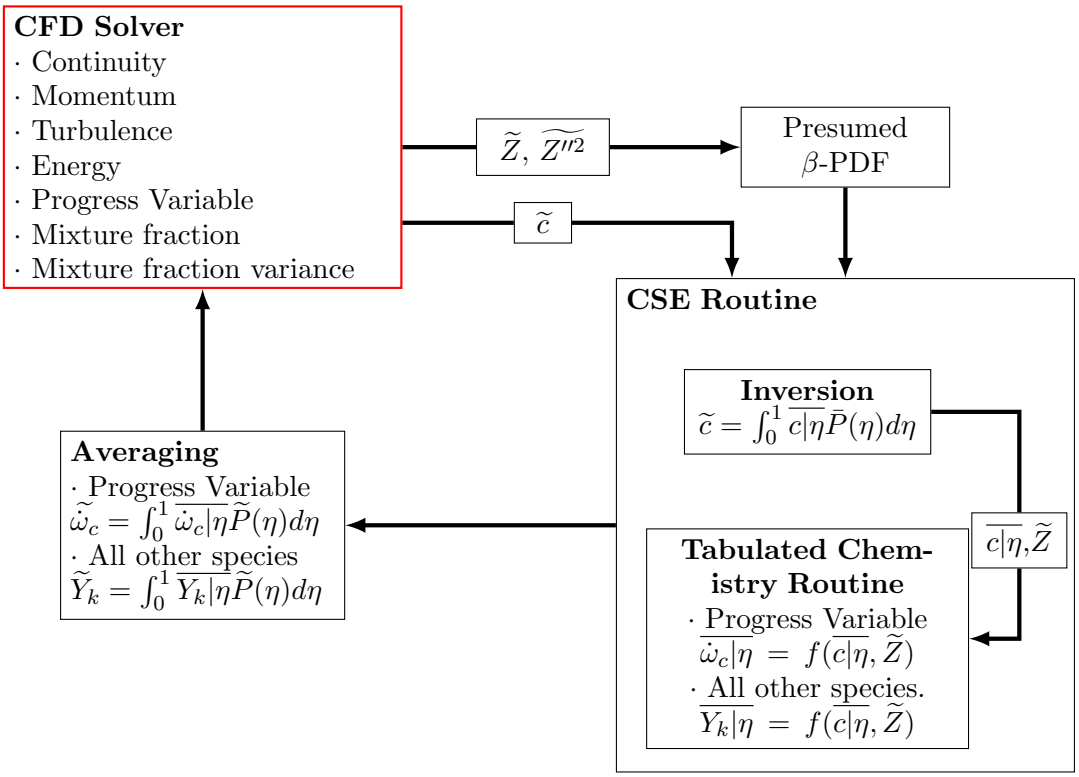

Figure 1. CSE Routine Structure

istry CSE to compare the results with DNS [23]. Later, a two-step reduced chemical kinetic mechanism was used to study a piloted methane/air diffusion flame [35]. These studies have shown reasonable agreement with DNS and experimental data and proved the predictive capabilities of CSE. Trajectory Generated Low-Dimensional Manifolds (TGLDM) were also found suitable for the simulation of methane-air flames in CSE context [36][30][37]. Preliminary studies have been performed using TGLDM on heavy fuels; however, the TGLDM calculation had to be aborted after ignition as the methane assumption used in generating the table was found to be invalid for n-dodecane after ignition [38]. Therefore, another low-dimensional manifold approach is needed for more complicated hydrocarbon fuels.

3.1. Flamelet Generated Manifold

In this study, chemistry is included in CSE using the Flamelet Generated Manifold (FGM) approach. The principle idea of FGM [4] is based on dimensional reduction techniques and flamelet models. In the FGM, the turbulent flame structure is described by pre-tabulating one-dimensional laminar flamelets using a reduced number of control variables. It decouples the solving procedure of the flame structure from the turbulent flow field by mapping the representative flamelet solutions onto a low-dimensional manifold in composition space. The resultant FGM table can be used to simulate multi-dimensional reacting flow without solving additional transport equations for all species. The flamelet equations, as given by Stahl and Warnatz [39], read:

$$\frac{\partial \rho}{\partial t} + \frac{\partial}{\partial x}(\rho u) = -\rho K \tag{12}$$

$$\frac{\partial \rho Y_i}{\partial t} + \frac{\partial \rho u Y_i}{\partial x} = \frac{\partial}{\partial x}\left(\rho D \frac{\partial Y_i}{\partial x}\right) + \dot{\omega}_i - \rho K Y_i \tag{13}$$

$$\frac{\partial \rho h}{\partial t} + \frac{\partial \rho u h}{\partial x} = \frac{\partial}{\partial x}\left(\frac{\lambda}{c_p}\frac{\partial h}{\partial x}\right) - \rho K h \tag{14}$$

$$\frac{\partial \rho K}{\partial t} + \frac{\partial u K}{\partial x} = \frac{\partial}{\partial x}(\mu \frac{\partial K}{\partial x}) + \rho_{ox} a^2 - \rho K^2 \tag{15}$$

where $K(x,t) = \frac{\partial u_y}{\partial y}$, is the strain rate or flame stretch field, which is a function of the x coordinate and the applied strain rate a at the oxidizer boundary. D is the diffusion coefficient defined as $D = \frac{\lambda}{\rho c_p}$. For non-premixed flames, a unity Lewis number is assumed in order to simplify the transport equations.

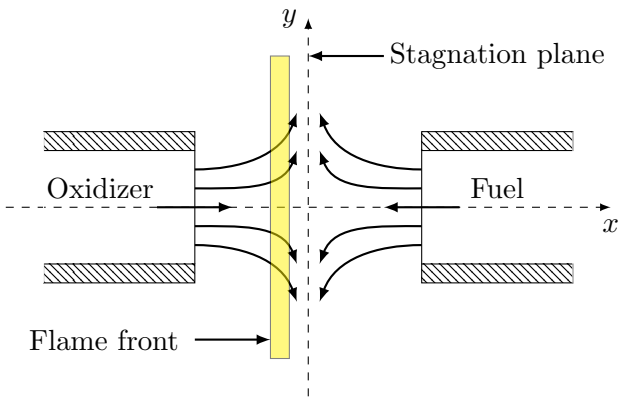

Figure 2. Schematic of laminar non-premixed counter-flow diffusion flame

Depending on the combustion application, a flame configuration must be selected to accurately represent the chemical processes taking place in the flame of interest. In this study, the choice of flamelet (shown in Figure 2) is that of a 1D non-premixed laminar igniting counter-flow diffusion flame (ICDF) with solutions computed in space and time using the Chem1D code [40]. As shown in Figure 3 (a), generating the manifold first starts with solving a transient counter-flow diffusion flame at a strain rate of $500s^{-1}$ from an initially mixed (green line), but non-reacting state and then tracking this flame (black lines) through ignition until quasi-steady state (red line) is achieved. Following this, steady state flamelets are solved from $500s^{-1}$ down to $1s^{-1}$ to complete the manifold close to chemical equilibrium. The choice of $500s^{-1}$ as the highest non-quenching strain rate was suggested by Wehrfritz *et al.* [41] who showed ignition delay times to be insensitive to strain rate in the range of

$a < 1000s^{-1}$. Bekdemir *et al.* [3] also found that for moderately strained configurations, a single unsteady flamelet was able to capture the ignition process adequately.

Once the flamelet solutions are computed, they are parametrized against mixture fraction, Z, and reaction progress variable, c, with a manifold resolution of 100x100 quadratically spaced points respectively (shown in Figure 3 (b)). Mixture fraction is described by the well known Bilger definition [42]. Quadratic spacing leads to refinement near the stoichiometric for mixture fraction and 0 for progress variable, ensuring interpolation accuracy during the early phases of ignition, as described by Eguz *et al.* [43]. The reaction progress is a monotonic variable that captures each stage of combustion evolution, which is defined as a linear combination of three key species (CO, CO_2 and CH_2O) normalized by their equilibrium value:

$$c = \frac{\sum \alpha_i Y_i}{\sum \alpha_i Y_i^{eq}} \tag{16}$$

The values of the weights in this study were kept at the default recommended values of CONVERGE-CFD. The inclusion of CH_2O is inspired by the notion that it is significant at the start of the ignition process, whereas CO represents the intermediate stage of combustion and subsequently CO_2 represents the end of the combustion process. It is to be noted here that the definition of progress variable will not affect results as long as the chemistry parameterization (selection of species) represents each stage of chemical evolution and is monotonic. The monotonicity of the progress variable is ensured during the parameterization process leading to a consistent FGM. A typical sub-space describing the FGM generation process is shown in Figure 4(a) and the resultant manifold is shown in Figure 4(b).

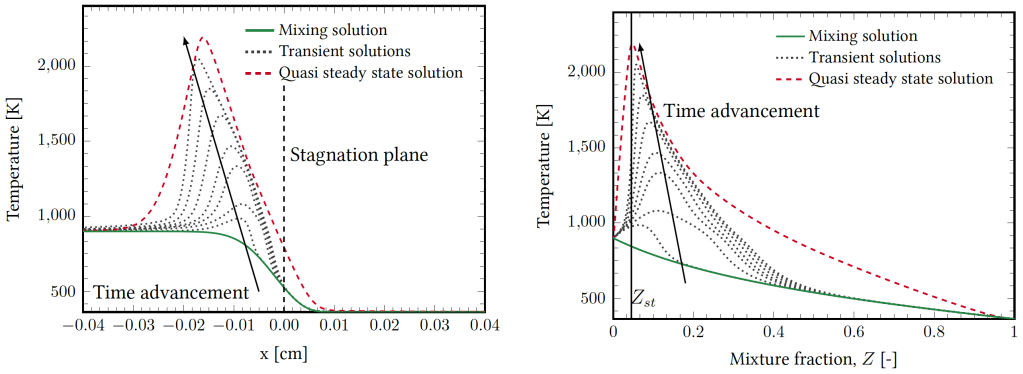

(a) Physical space

(b) Mixture fraction space

Figure 3. Temperature evolution for an igniting counter-flow diffusion flame with n-dodecane: a=500 s^{-1}, T_{fuel}=363 K, T_{Ox}=900 K, P_{amb}=6.0 Mpa (a) physical space (b)mixture fraction space

4. Computational Setup

Simulations are performed for the ECN "Spray A", and the results are validated against the ECN's high-quality and high-fidelity data-sets. "Spray A" is a low-

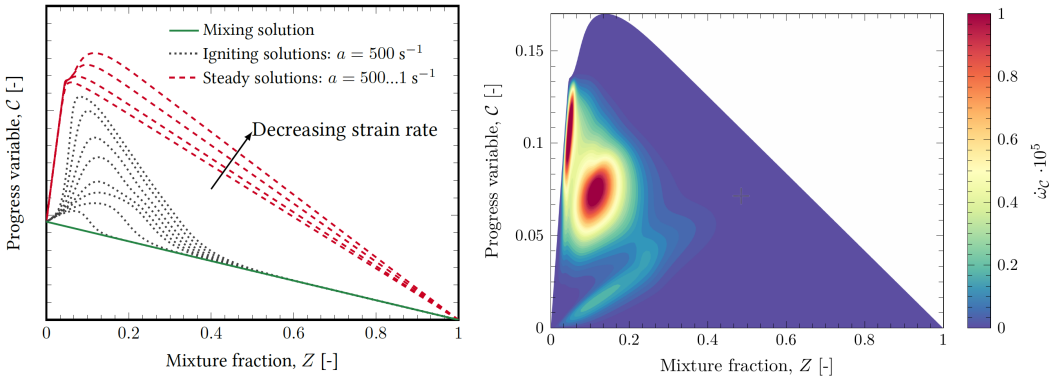

(a) (b)

Figure 4. (a) Schematic representation of progress variable as a function of mixture fraction (b) Reaction rate as a function of progress variable and mixture fraction

temperature combustion condition relevant to engines that use moderate EGR and have minimal NOx emissions. The injector specifications pertain to modern advanced injection systems with high pressure capability. Both non-reacting and reacting conditions for "Spray A" tested in this study are listed in Table 2.

Table 2. "Spray A" Boundary Conditions

Test Type	**Non-reacting**	**Reacting**
Fuel surrogate	n-dodecane	
Injection Pressure (bar)	1500	
Fuel Injection Temperature (K)	363	
Nozzle Diameter (μm)	84	
Injection Duration (ms)	1.5	
Injection Mass (mg)	3.5	
Ambient Gas Composition [by vol.]	0% O_2 89.71% N_2 3.77% H_2O 6.52% CO_2	15% O_2 75.15% N_2 3.62% H_2O 3.62% CO_2

The computational setup for RANS is identical to that provided in [28], therefore in this section, only the LES computational setup will be detailed. For LES simulations in this study, the one-equation, viscosity-based LES model was used. This involves using the sub-grid turbulent kinetic energy, k_{sgs} to compute the turbulent viscosity as:

$$\nu_t = C_k k_{sgs}^{\frac{1}{2}} \Delta \tag{17}$$

where C_k is a model constant, commonly set to 0.05, and Δ is the cube root of the cell volume. The sub-grid kinetic energy $k_{sgs} = \frac{1}{2}\left(\widetilde{u_i u_i} - \tilde{u}_i \tilde{u}_i\right)$, is modelled with a transport equation developed by Yoshizawa *et al.* [44] and Menon *et al.* [45] as:

$$\frac{\partial \bar{\rho} k_{sgs}}{\partial t} + \frac{\partial \bar{\rho} \tilde{u}_i k_{sgs}}{\partial x_i} = -\tau_{ij} \frac{\partial \tilde{u}_i}{\partial x_j} - \epsilon + \frac{\partial}{\partial x_i}\left(\bar{\rho} \frac{\nu_t}{\sigma_k} \frac{\partial k_{sgs}}{\partial x_i}\right) \tag{18}$$

The sub-grid stress tensor is calculated using:

$$\tau_{ij} = -2\nu_t \tilde{S}_{ij} + \frac{2}{3} k_{sgs} \delta_{ij} \tag{19}$$

where $\tilde{S}_{ij}$ is the strain rate tensor and δ_{ij} is the Kronecker operator. The sub-grid dissipation in this model, ϵ_{sgs} is given as:

$$\epsilon_{sgs} = C_\epsilon \frac{k_{sgs}^{\frac{3}{2}}}{\Delta} \tag{20}$$

where C_ϵ is a model constant, typically set to 1.

In LES, the mixture fraction variance can be approximated through a dynamic model:

$$\widetilde{Z''^2} = C_{var} \Delta^2 \left| \frac{\partial \widetilde{Z}}{\partial x_j} \right|^2 \tag{21}$$

where C_{var} is a dynamically computed model coefficient [46].

The computational domain for both RANS and LES are identical. The injector is positioned centrally with injection into the axial direction. All boundaries are set as non-slip walls with a constant temperature of 461 K as measured in the experiment. The simulation conditions are set to the 900 K ECN "Spray A "baseline conditions. The injector nozzle diameter is 0.084 mm with a discharge coefficient of 0.89 corresponding to "Spray A" injector 210677 [47]. For LES, a structured grid is generated at runtime with a base cell size of 1.4 mm. Adaptive mesh refinement is enabled based on both velocity (0.1 ms^{-1}) and temperature (5 K) fluctuations with a minimum cell refinement of 0.0875 mm. Furthermore, a conical fixed grid refinement of 0.0875 mm is placed along the injector axis to resolve this high velocity region better. In order to maintain a reasonable runtime, the maximum cell count is limited to 2.6 million cells. These cell sizes were determined through a grid dependence study conducted under non-reacting conditions of the spray. Further details will be presented in Section 5.1. A section of the computational domain showing the grid and cell refinement can be seen in Figure 5.

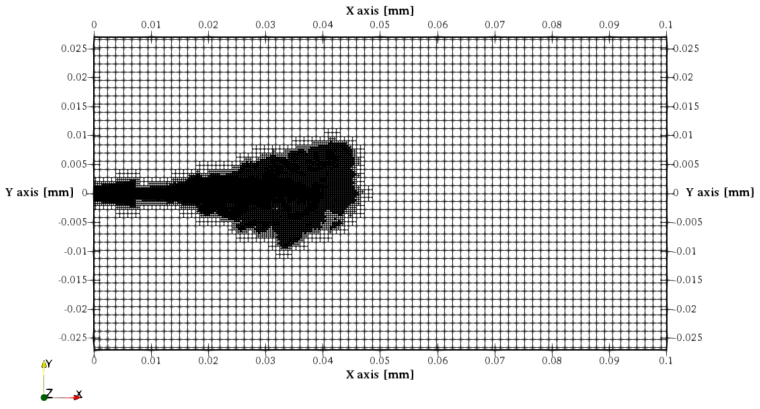

Figure 5. Spray computational domain with grid refinement methods.

5. Non-reacting Spray

5.1. LES Grid Dependence

The non-reacting spray simulation process is similar to the RANS solving process where a grid dependence study of the LES computational setup was first conducted. The mesh size of the LES sensitivity study was varied from 0.125 mm to 0.0625 mm. The detailed grid setup for grid dependence test is given in Table 3. For the study of LES grid dependence, only a single realization for each grid is computed. Previously, Xue *et al.* [48] examined how LES grid resolution and sub-grid model performance affects fuel spray simulations under non-reacting conditions. They found that for the prediction of global spray characteristics, a single LES realization can sufficiently represent the ensemble-averaged values. For all grid sizes, the liquid penetration shown

Table 3. LES grid dependence parameters.

Grid	Coarse	Medium	Fine
Min cell size [mm]	0.125	0.0875	0.0625
Spray parcels$\cdot 10^6$ [-]	0.8	2.4	3.2
Max cell number$\cdot 10^6$ [-]	1.4	2.6	5.0
Core-hours for 1 ms [-]	252	672	1440

in Figure 6 is seen to be more sensitive during the transient period of the spray. A similar trend is observed for the RANS simulations previously shown in [49] where, for the coarse grid, the liquid penetration spikes around 0.2 ms, although significant differences were observed for the RANS non-reacting simulations at steady state for the coarse grid. The LES simulation results are compared to experimental data over the injection duration where the liquid penetration is shown to be insensitive to grid size after the transient period. Compared to liquid penetration, vapour penetration is more sensitive to grid sizes. Figure 6 shows the vapour penetration for all grid sizes where both medium and coarse grid size overpredicted the vapour penetration length. An improved prediction is achieved when using the finest grid size of 0.0625 mm. However, the medium grid size of 0.0875 mm also shows good agreement with the experimental measurements after 0.5 ms. For the balance of computational cost and accuracy, a grid size of 0.0875 mm was chosen for further studies. Similar grid sizes for LES diesel spray simulation can found be in the literature [46].

5.2. Non-reacting Vaporising Spray

The non-reacting spray studies also follow a similar process as the RANS studies shown in [27]. However, for LES simulations, it is necessary to simulate multiple realizations or perform temporal averaging in order to obtain statistically relevant averaged quantities. Senecal *et al.* [50] simulated ECN "Spray A"with 20 LES realizations and the results indicate that having nine realizations is a large enough sample to capture experimental velocity and mixture fraction distribution with mean absolute errors of 2.0 ms^{-1} and 0.005 respectively around 95% of the time. A more recent study from Pei *et al.* [46] found that with five LES realizations a 98% to 99% similarity to an equivalent of 16 LES realizations for larger scale fluctuations (e.g. mixture fraction and velocity magnitude) and temperature can be achieved. For variables with shorter scale fluctuations, more LES realizations are necessary. Blomberg *et al.* [16] also used 5 realizations for each case under engine relevant conditions for a split injection diesel spray to cap-

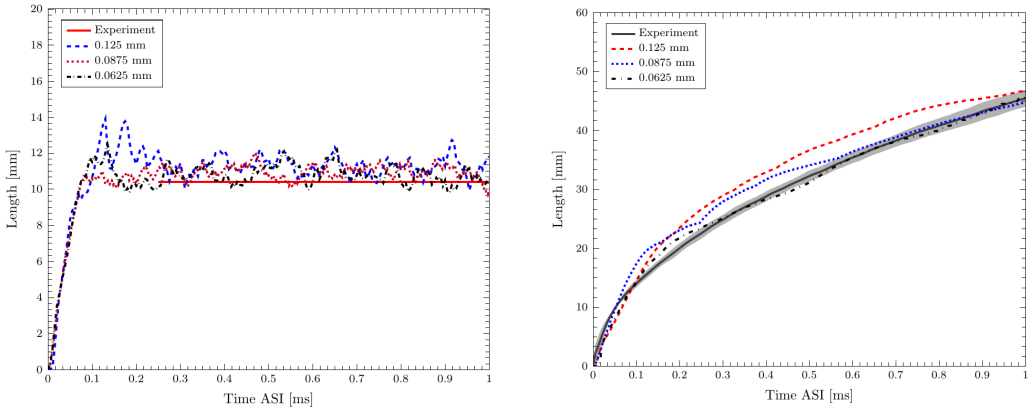

Figure 6. Liquid (a) and vapour (b) penetration length as a function of grid size. Liquid length is defined as the axial location of 99% liquid mass threshold. Vapour penetration is given as the maximum distance from the injector to where the fuel mass fraction is 0.001.Experimental data repeated from [47]

ture the combustion recession at the end of injection. Ameen *et al.* [51] simulated 5 realizations and took advantage of the axisymmetry of ECN "Spray A"and performed spatial averaging on 35 planes in the azimuthal direction, leading to self-similar profiles for mixture fraction, temperature, OH and soot. As expected, centreline profiles still showed large variance compared to the experiment as there are only five samples with all azimuthal planes sharing the same centreline. Further improvement in statistical convergence can be obtained by also applying time averaging once the jet has reached quasi-steady state; in non-reacting conditions, this can be considered the time after the gas jet has stabilized and in reacting conditions, the time after which the flame lift-off length has stabilized.

Before discussing the details of simulation results, it is worth noting that stabilization of the gas jet is measured as the time when the head of the jet passes out of the test section. The test section is chosen to match the experimental test window, which is from 17.85 mm to 50 mm in the axial direction. In the experiments, mixture fraction is measured using Rayleigh Scattering with samples captured at long delays (3.2-7.0 ms) after the start of injection and ensemble averaged over 20-40 injections, depending on the test condition [52]. This is to ensure the measured jet is at steady state, so that jet transients do not affect measurements. Experimental velocity measurements are taken with time-resolved PIV and ensemble averaged over approximately 20 injections at defined time instances after the start of injection [53]. Velocity measurements in the near nozzle region are not considered accurate as the proximity of the liquid jet generates high intensity Mie scattered light that interferes with tracer particle imaging. Additionally, the PIV particle density is too low in this region as not enough particles have been entrained in the spray. As such, only velocity measurements downstream of $x = 20$ mm will be considered.

As it is computationally prohibitive to run simulations for long durations (3.2-7.0 ms) as in the experiment, as well as quasi-steady state experimental reacting data being available before 1.5 ms – the following three approaches are used to validate the computational model with experimental measurements:

- Mixture fraction: temporal and spatial averaging of 5 LES realization using 25

temporal samples between 1.5-2.0 ms and 12 azimuthal planes for each sample.

- Velocity field: ensemble and spatial averaging of 5 LES realizations and 12 azimuthal planes for each realization at 1.0 ms ASI.
- Temperature field: ensemble and spatial averaging of 5 LES realizations and 12 azimuthal planes

Each LES realization has been perturbed by varying a random number seed that is input into the random number generator within the injection model. Varying the random number seed will change the initial position and velocity of an injected spray parcel. Whilst this method of perturbation is purely numerical, using a random number seed is expected to account for the variations observed from one injection event to another. Furthermore, it was found by Ameen *et al.* [51] that results from random number seed perturbations were comparable to perturbations originating from varying the initial turbulence intensity. Figure 8 qualitatively shows the difference in mixture fraction distribution between the 5 realizations. Spatial averaging is applied in the azimuthal direction for each realization, as illustrated in Figure 7. Each plane is 60 mm long and 30 mm wide, which is then discretized by 0.08 mm to preserve resolution.

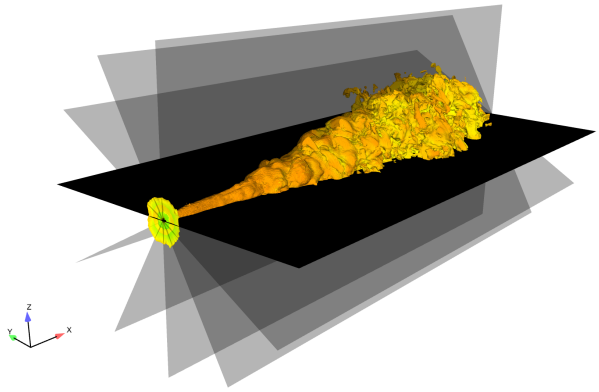

Figure 7. ISO volume of spray jet showing azimuthal averaging planes.

In this study, the liquid penetration length is given as the axial distance from the nozzle tip to the location of liquid fuel encompassing 97% of the injected fuel mass. And the vapour penetration is given as the maximum distance from the injector to where the fuel mass fraction is 0.001. Figure 9 shows the liquid and vapour lengths for both simulations and experiments. Only a mean value of liquid length is available from the experiment which matched very well with the LES model predictions. Vapour penetration length is slightly overpredicted by the LES model early in the injection duration. However, after 0.5 ms, the simulation is in good agreement with the mean experimental measurement.

The axial mixture fraction distribution is presented in Figure 10(a) where it can be seen that the averaged simulation result underpredicts mixture fraction compared to the experiment across most of the axial length. The standard deviation between simulation and experiment is comparable, and the predicted results fall within experimental variance. These results are consistent with LES studies of this experimental test point in the literature that use similar models and grid resolution [41, 50]. The underprediction in centreline mixture fraction is likely attributed to the early sampling time in the simulations [50]. As experimental mixture fraction is measured at

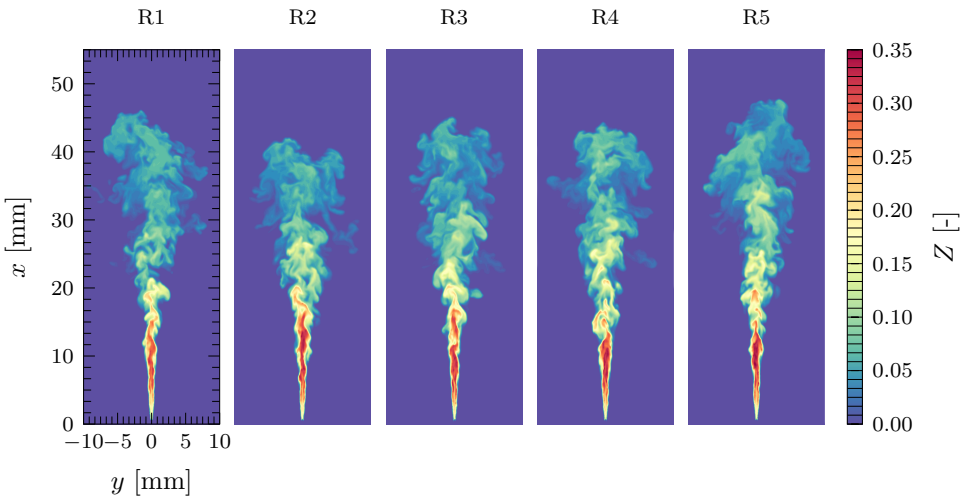

Figure 8. Mixture fraction distribution at 1.0 ms ASI for 5 LES realizations perturbed by a random number seed.

long delays (3.2-7.0 ms) after the start of injection, the mixture fraction field has not fully developed in the simulations, which are only run until 2.0 ms. Furthermore, Wehfritz has reported that increased spatial resolution (47.5 μm) resulted in improved centreline mixture fraction predictions. This has not been investigated due to the high computational cost. The velocity fields which are sampled at the same time instance after the start of injection (1.0 ms) between simulation and experiment are shown in Figure 10 (b). There is good agreement between the ensemble averaged simulations and experimental measurements across the axial distance. As expected, simulation variance is high due to the low number of samples (5).

From Figure 11, it can be seen that the radial profiles of simulated mixture fraction and velocity are in good agreement with experimental measurements at all axial locations. These axial locations have been selected as the experimental lift-off measurements fall between 8-30 mm (non-reacting data is unavailable for $x < 17.85$ mm). Accordingly, there is an underprediction in centreline mixture fraction; however, mean and variance predictions are improved at locations away from the centreline.

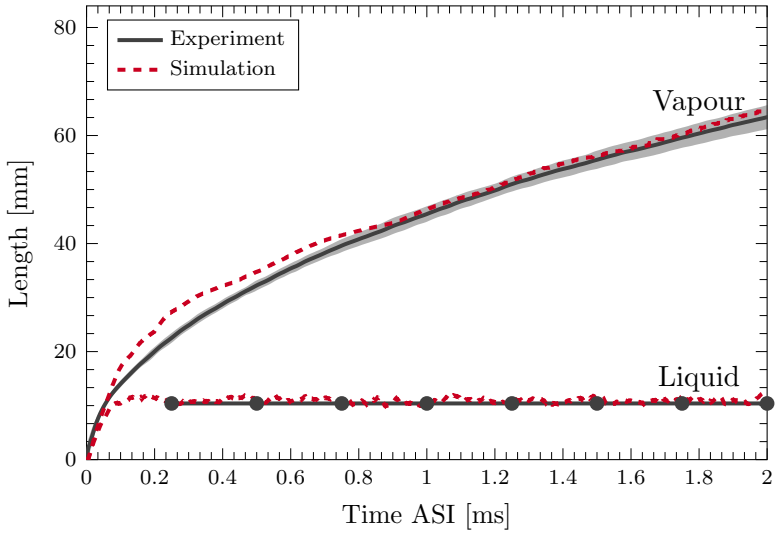

Figure 9. Experimental and simulation penetration lengths. Vapour length is defined as the axial location of 1% vapour mass threshold. Liquid length is defined as the axial location of 99% liquid mass threshold. The shaded area represents experimental uncertainty.

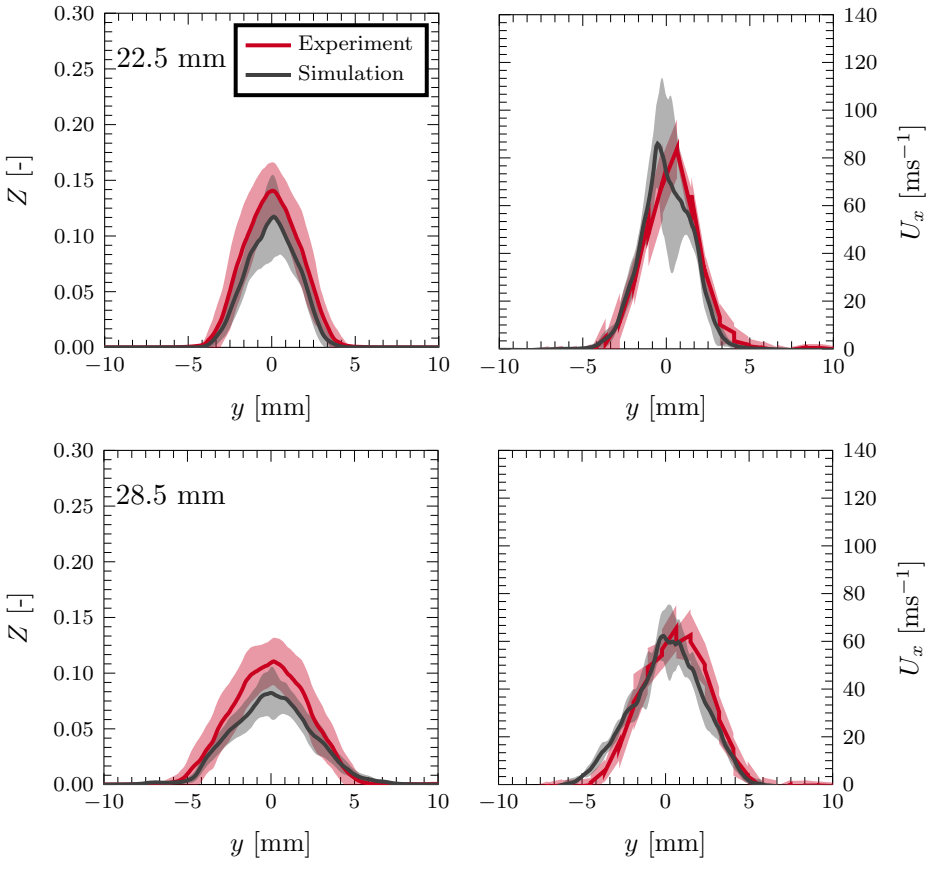

Figure 11. Radial profiles of mixture fraction (left) and axial velocity (right) for experiment and simulation at three axial positions. The shaded area represents standard deviation.

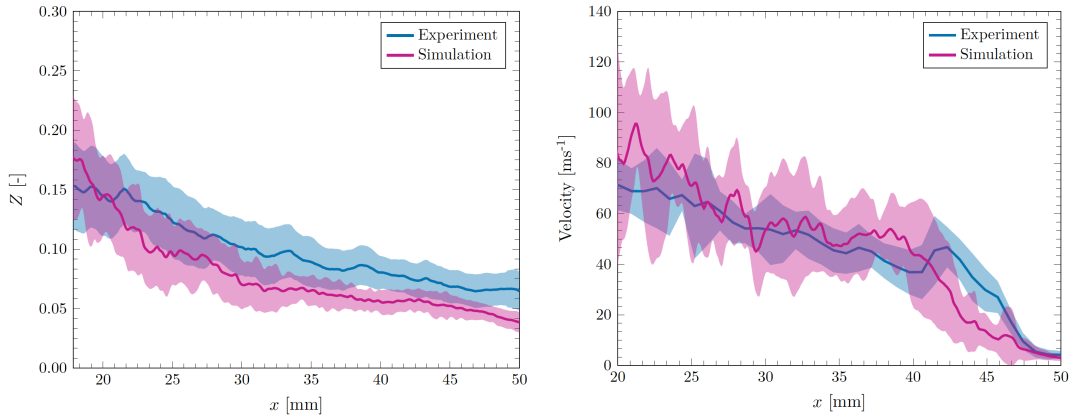

Figure 10. Axial comparison of experimental and simulation (a) mixture fraction distribution and (b) velocity fields at 1.0 ms ASI. The shaded area represents standard deviation.

6. Reacting Spray Study

In this section, the validation and comparison of combustion models are carried out following the ECN modelling standards. Simulations are performed using the reduced n-dodecane kinetic mechanism of Yao *et al.* [54]. Before conducting the 3D simulation of diesel spray using the above chemical mechanism, a mechanism validation test is conducted in terms of the ignition delay times for homogeneous mixtures with varying equivalence ratios and initial temperatures. The same tests were conducted by Yao *et al.* [54] during the development of the skeletal mechanism; however, the current study is completed using the CONVERGE 0D chemistry tool and its ODE solver, therefore confirming the numerical consistency of the current study is important. Figure 12 (a) shows the ignition delay time comparison between CONVERGE 0D results and the available shock tube experimental results from Vasu *et al.* [55] at 20 bar. The results are consistent with those obtained by Yao *et al.* [56] where, at higher temperatures, there exists an overestimation of the ignition delay time, and at lower temperatures, the mechanism provides a reasonable prediction of the experiments. For engine relevant conditions (60 bar), similar 0D studies were also conducted, which are not included in this paper. In order to further explore the capabilities of the mechanism, a study of the flame was carried out using the 1D chemistry solver CHEM1D under the investigated 3D simulation conditions. Figure 12 (b) depicts the temporal evolution of the maximum temperature over the duration of injection. The results indicate that the current mechanism is capable of capturing different stages of low temperature combustion. Both the first stage and second stage ignition are substantially increased by the reduction of ambient gas temperature. This observation is consistent with previous flamelet calculations [28] and simulation studies using reduced chemistry [41].

6.1. Flame Temporal Evolution and Ignition Study

Table 4 quantitatively shows the comparison of measured and simulated ignition delay time (IDT) and flame lift-off length (LOL) at “Spray A” baseline conditions. According

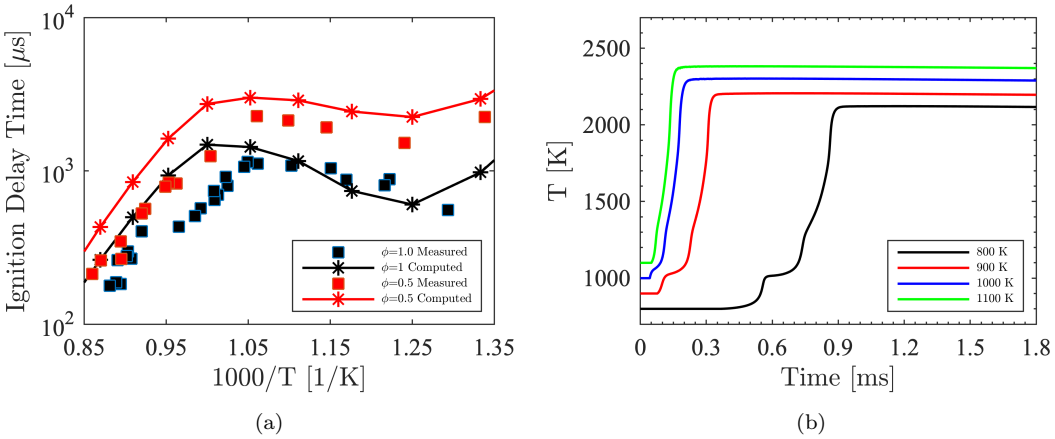

Figure 12. Chemical kinetics studies (a) Comparison between measured ignition delay times for n-dodecane [55] and computed values from CONVERGE 0D chemistry solver using Yao mechanism at $p = 20$ bar and $\phi = 0.5$ and $\phi = 1.0$ [56] (b) Maximum temperature evolution of Yao mechanism under investigated conditions using 1D-FGM.

to the recommended ECN guidelines, the ignition delay time is calculated as follows:

$$\tau_{IDT} = \tau(max(\frac{dT_{max}}{dt})) - \tau_{SOI} \tag{22}$$

The definition of flame lift-off length used in this work is also consistent with the ECN standard for simulations and is thus defined as the distance from the injector to the first location where the Favre-averaged OH mass fraction reaches 14% of the instantaneous maximum during the steady state period. It can be seen that both the CSE-FGM RANS and LES simulations are able to successfully capture both combustion metrics to a high degree of accuracy. For the RANS study, a slight overprediction is observed for flame lift-off prediction. Additional parametric studies were conducted under the RANS framework for validation. Figure 13 shows the ignition delay time and flame lift-off length predictions of CSE-FGM model compared to the experimental studies and well-stirred reactor model available in CONVERGE CFD. Both combustion models are able to capture the trend of ignition delay under different ambient temperature conditions where ignition is prolonged when the ambient temperature is lower. Similar trends for flame lift-off length under various ambient temperature is also predicted by the two combustion models. An overprediction in both the IDT and the LOL is seen for well stirred reactor (WSR) combustion model with more visible discrepancy observed at lower ambient temperature. Previous studies have found the inclusion of turbulent chemistry interaction and sub-grid variance plays an important role at low temperature ignition [57][46]. With the current CSE routine including both of these terms, both first and second stage ignition can be more accurately captured under low-temperature conditions. To further study the CSE-FGM model characteristics, more details are given for baseline conditions under "Spray A" conditions due to more comprehensive experimental dataset available and more LES realisations performed.

Figure 14 and 15 show the temporal evolution of mixture fraction and temperature

Table 4. Ignition delay time and flame lift-off length for ECN "Spray A" baseline condition. Experimental data repeated from [47].

Baseline (900 K, 15% O_2)	Experiment	CSE-FGM/LES	CSE-FGM/RANS
Ignition delay time [ms]	0.40-0.44	0.408	0.413
Flame lift-off length [mm]	15.80-17.90	18.08	19.31

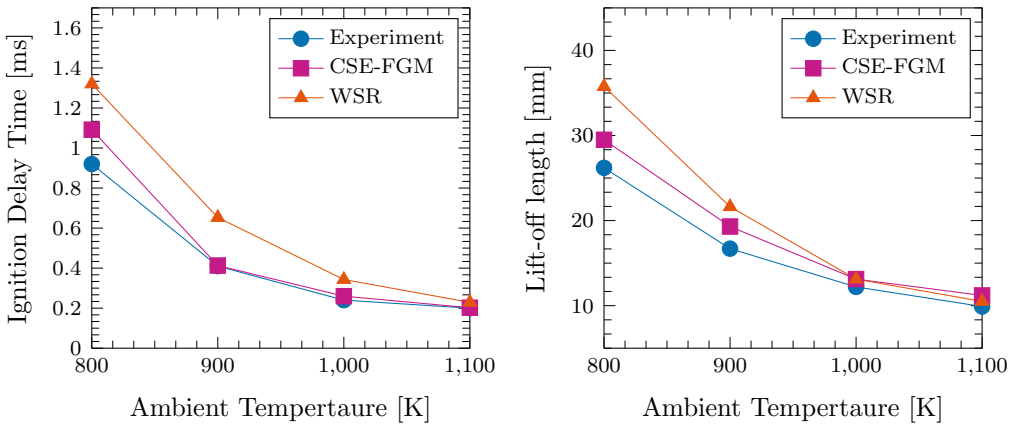

Figure 13. Parametric studies of RANS CES-FGM at different ambient temperature compared with the mean experimental results and homogenous reactor results for ignition delay time (left) and flame lift-off length (right)

field between RANS and a representative realisation of the five LES calculations for the ECN "Spray A" 900 K baseline condition. The black lines in Figure 15 represent the stoichiometric mixture fraction (Z_{st}=0.045). It can be observed from both figures that a significant fluctuation of mixture fraction and temperature field is present in the LES simulations compared to those of RANS simulations at the same timestep. This can result in different ignition behaviour, which will be examined in detail later. It is also worth noting that for RANS simulations the Z_{st} line crosses the middle of the high temperature field, which is closer to the jet centerline, overlapping more of the high temperature region compared to LES simulation. The LES Z_{st} line is located at the edge of the flame where high temperature reactions exist. The reason for this is that the LES simulation is a single realisation with spatial averaging, which results in a thin flame due to a very fine mesh. In contrast, RANS is an ensemble averaged simulation which thickens the flame and moves the Z_{st} line to the centre of the flame. Ensemble averaged LES results will be discussed later.

Previous experimental studies have identified that the combustion of a diesel spray can be divided into two stages [58]. Due to the complex physical processes included in the spray combustion modelling, understanding autoignition or two-stage ignition processes is very challenging. Therefore the capability of CSE-FGM combustion in capturing this critical event is further investigated. The first stage of ignition in this study is defined as events where the temperature rise is less than 400 K above the ambient temperature, therefore making it easier to distinguish from the main high temperature combustion event. In order to better illustrate the typical two-stage ignition behaviour of n-dodecane, Figure 16 divides the LES simulated flame evolution into two different parts. At 0.30 ms ASI, a slight increase of temperature is observed

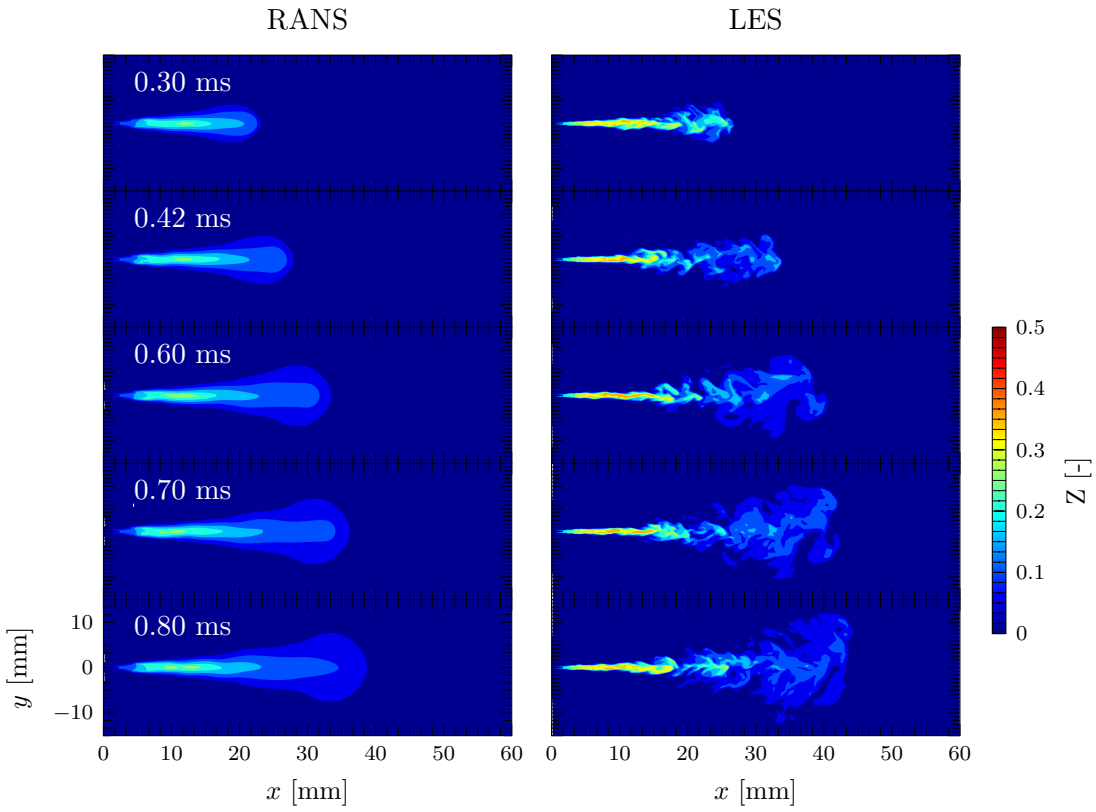

Figure 14. Instantaneous mixture fraction fields for CSE-FGM RANS (left) and LES (right) simulations at the 900K "Spray A " baseline condition. The time after start of injection is shown at the top left of image.

at the outer edge of the jet (Z_{st}) around 20mm downstream of the nozzle. This can be seen as the beginning of low temperature reactions where low temperature heat release is observed. The onset of second-stage ignition takes place approximately at 0.40 ms ASI and occurs in the head of the jet where the velocity magnitude is relatively low. The vapour temperature here rises 300-400 K above the ambient temperature, and volumetric ignition takes place with multiple ignition kernels. The higher temperature region (around 1000K) region exists entirely within the Z_{st}. This is followed by the expansion of a high temperature diffusion flame (0.6-0.8 ms), which eventually stabilizes downstream of the injector. It can be observed from Figure 15 that at around 0.7 ms, the flame has approached quasi-steady state. This finding is consistent with the results from other studies [51][54]. Additionally, at approximately $x = 30$ mm, the diffusion flame begins to thicken radially. This phenomenon has been observed in previous studies [46] and is attributed to the recirculation zone behind the head of the jet. These vortices enhance turbulence levels locally and lead to the thickening of the flame in this area.

Following the study of flame spatial transient behaviour, the temporal evolution of the scatter plot of temperature in mixture fraction space are given in Figure 17. The PDFs of mixture fraction during ignition are also shown in Figure 17 at two LES time instances near ignition (t=0.40 ms and t=0.44 ms). For both RANS and LES at 0.19 ms, all the points are clustered around the mixing line. Prior to second stage combustion, at around 0.40 ms, both RANS and LES points show a higher

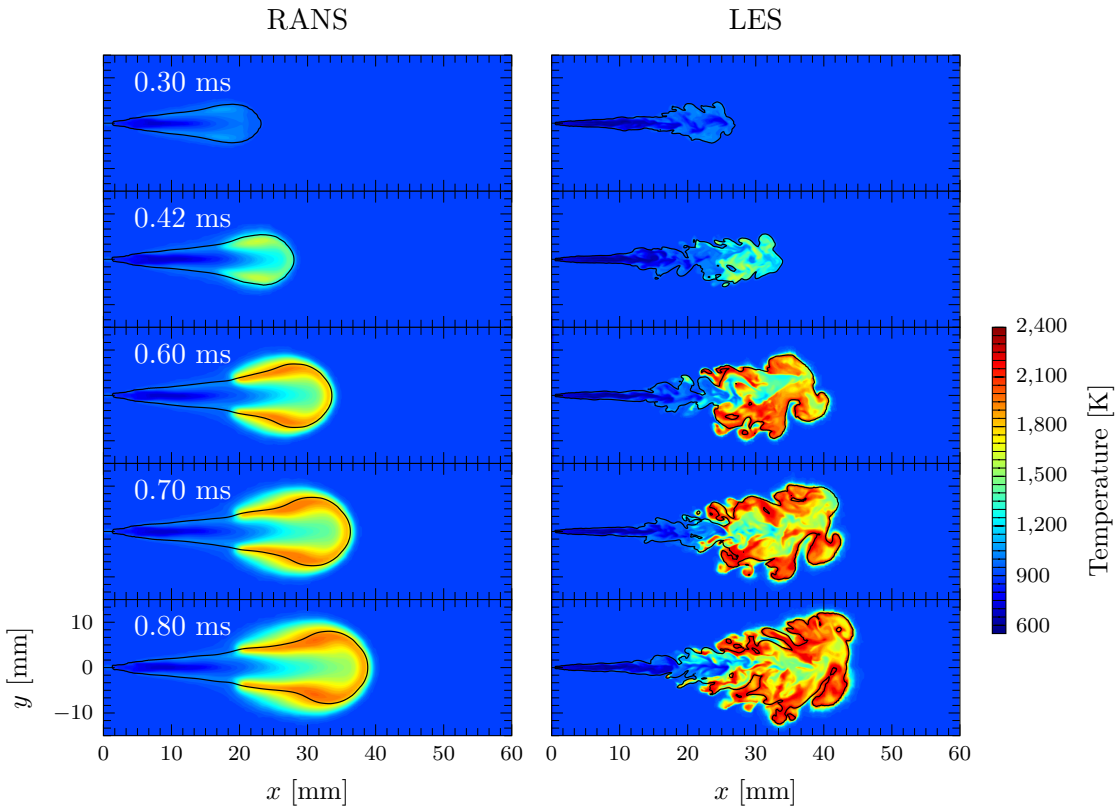

Figure 15. Instantaneous temperature fields for CSE-FGM RANS (left) and LES (right) simulations at the 900K "Spray A " baseline condition. The time after the start of injection is shown at the top left of the image. The black line is the stoichiometric mixture fraction contour

temperature in rich mixtures at around Z=0.11. The LES PDF further demonstrated the characteristics of ignition taking place under fuel-rich conditions. Minor species are also given here to assist the study of ignition behaviour. It is worth noting that LES predicts an abrupt transition in the mixture fraction space for certain temperatures during the main combustion stage (shown in the edge of Figure 17), whereas RANS gives a smoother transition of temperature at different mixture fractions. This is likely due to the single LES realisation that promotes an abrupt transition in the ignition process. For RANS, the "ensemble averaging" process likely smooths out this apparent abrupt transition. At second stage combustion, both RANS and LES show that the combustion event favours a mixture fraction less than 0.15. The temperature continues to rise, and the mean temperature approaches that of the equilibrium state.

To further the understanding of n-dodecane spray ignition processes, several key intermediate species, such as hydrogen peroxide (H_2O_2), hydroxyl (OH) and formaldehyde (CH_2O) were included alongside the LES temperature-mixture fraction plot in Figure 18. The solid black lines indicate the position of stoichiometric mixture fraction. The combustion process of n-dodecane follows [59], where the generation of H_2O_2 and CH_2O is identified as the first stage of ignition, and the disappearance of H_2O_2 and the formation of OH are identified as the second stage ignition. With these chemical properties in mind, at 0.19 ms, low temperature reactions have been initiated at the edge of spray jet. These reactions first occur in leaner mixtures as these are at the highest temperature in the unburnt flow field. Figure 18(i) shows

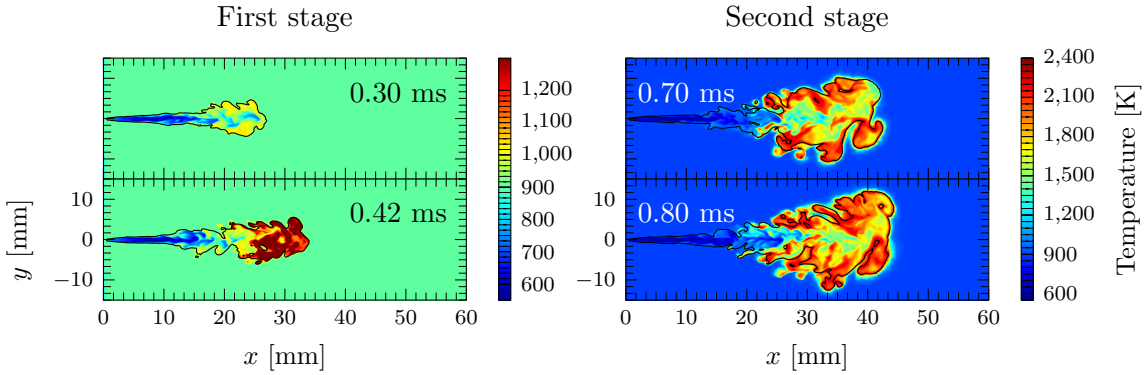

Figure 16. LES Contour plot of temperature for first stage (left) and second stage(right) ignitions at the 900K "Spray A" baseline conditions. The black line represents Z_{st}

a minor increase in conditional temperature at 0.19 ms ASI . At 0.30 ms ASI, first stage ignition is underway as indicated by the increase in formaldehyde mass fraction. The low temperature reactions, here coupled with the high scalar dissipation rate in this region, initiate a turbulent cool-flame which transports species and heat release to colder and richer mixtures. This is demonstrated by the shift in conditional temperature (ii), from leaner to richer mixtures. This is also consistent with Figure 16, where ignition happens in a lean mixture and the high temperature region expands and penetrates into a more fuel-rich mixture. Second stage ignition is initiated with multiple high temperature points seen over a broad range of rich mixture fractions. The consumption of hydrogen-peroxide at the head of the spray also signifies the onset of second-stage ignition as its decomposition is critical in promoting high temperature reactions. At 0.44 ms, the highly stratified flow field, formed from high temperature ignition, initiates turbulent flame propagation (iii) from richer to leaner mixtures. The consumption of formaldehyde and hydrogen-peroxide are clearly seen at the head of the spray. Additionally, the decomposition of H_2O_2 to OH and its associated hot-spots confirm the occurrence of high temperature reactions and volumetric ignition. This follows a previous numerical study of a non-premixed flame, where, following a localised autoignition event, the reaction zone will propagate around the kernel [60]. It is also clearly seen that several ignition spots are observed inside the rich mixture region; these spots then expand and finally connect at a later stage. The ignition behaviour and temporal flame structure presented here are consistent with previous experimental studies [61][52][47] and numerical studies [46] [14].

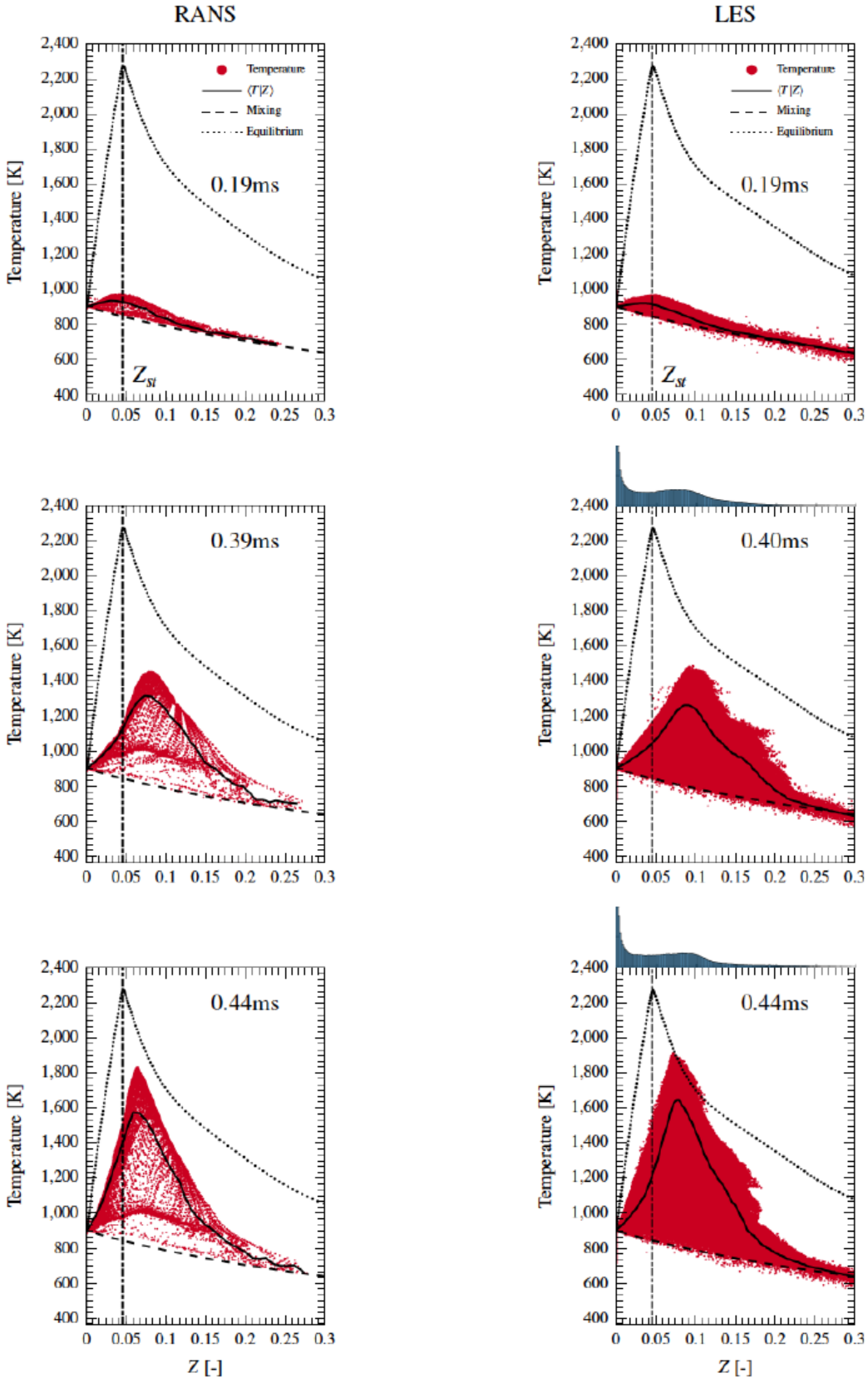

Figure 17. Temporal evolution of scatter plot of temperature versus mixture fraction between RANS (left) and LES (right, marginal PDFs of mixture fraction are included for two time instances) for the 900K "Spray A" baseline condition.

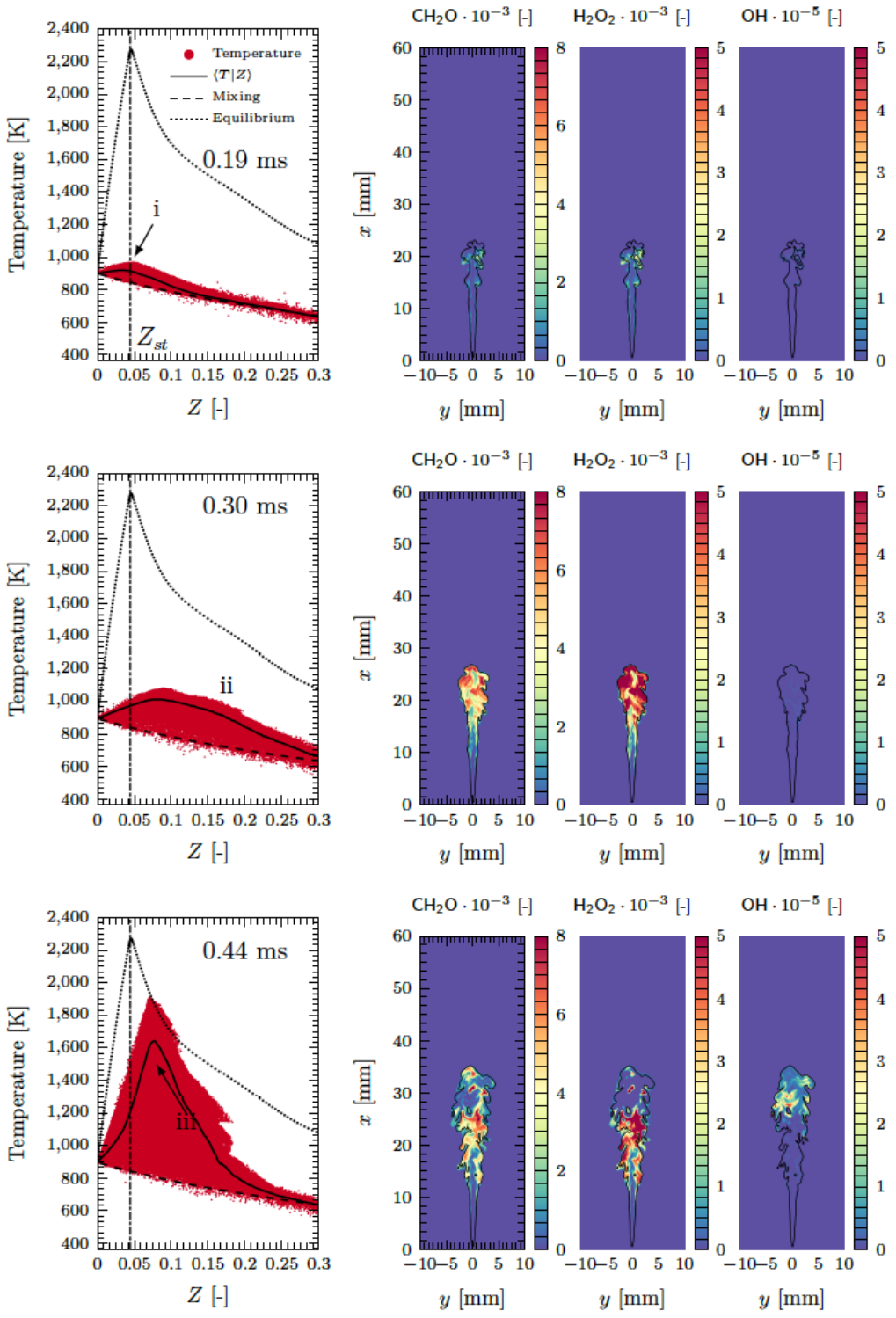

Figure 18. Scatter plot in Z-T space with X-Y cut-planes of (1) Formaldehyde, (2) Hydrogen-peroxide and (3) Hydroxyl. The solid black line in cut-planes is the contour of stoichiometric mixture fraction.

While the previous discussion of flame temporal evolution and ignition concentrated only on the analysis of the computational results, it is also possible to compare the simulation results with experimental results. Due to the difficult conditions of this flame, limited experimental information is available. Various diagnostic techniques were used in different institutions, such as high-speed schlieren, Mie-scattering and chemiluminescence imaging. Despite substantial efforts in experimental studies, only partial sets of data can be provided, with only one or two species available simultaneously. Quantitative experimental measurements of local mixture-fraction, species mass fractions, velocity field and temperature field are not yet available for reacting conditions. For the study of flame temporal evolution, Figure 19 shows the experimental schlieren images for the 900 K standard "Spray A" conditions. To aid the visualisation of the high temperature reaction, the border of the high-temperature chemiluminescence (blue line) is overlaid on the simultaneously-acquired schlieren images. The details of image processing and experimental set up can be found in [62]. Even if a quantitative assessment is not possible, the computed distributions from LES shows a good agreement throughout the evolution of the flame.

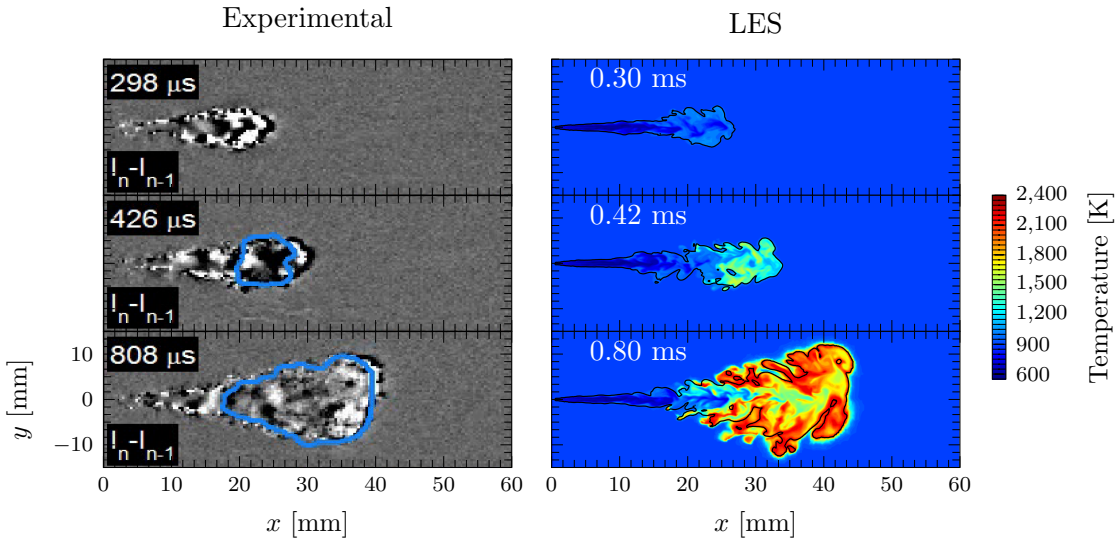

Figure 19. Schlieren image (left) and instantaneous temperature fields for CSE-FGM LES (right) simulations at the 900K "Spray A" baseline condition. The time after the start of injection is shown at the top left of the image. The blue line in the experimental study shows the luminosity border. The black line is the stoichiometric mixture fraction contour. The experimental images are corrected by its background intensity (I_n-I_{n-1}).

In order to compare the diesel spray ignition behaviour between the experimental data and the simulation result, the formaldehyde (CH_2O) field is presented. Skeen *et al.* [63] performed simultaneous single-shot planar laser-induced fluorescence (PLIF) and Schlieren imaging on the 900K "Spray A " baseline condition. Figure 20 shows the experimental spatial distribution of formaldehyde (left) from a single injection and a single LES realisation of formaldehyde concentration (right). As the PLIF results from the experiments are qualitative, no quantitative comparisons can be made at this point. Initial formaldehyde formation was observed at the periphery of the penetrating jet, followed by convection to the core. This corresponds to the first stage ignition and heat release. In the CFD simulations, the initial formation of formaldehyde is seen near the periphery of the jet at approximately the same location. This is followed by the penetration of the jet with high concentration CH_2O regions forming due to convection

along the centerline of the nozzle. The subsequent consumption of CH_2O corresponds to the main ignition event, and the high CH_2O concentration region stabilizes at a certain distance from the nozzle. The CFD model is able to predict the same trend. The high concentration region in simulations is predicted a few millimetres downstream in comparison to the experiments. This is related to the fact that the model is slightly overpredicting the lift-off lengths at this condition and is also subject to variations in multiple realisations. It must be noted that the experiments were carried out for a single injection event. The resolution in the CFD grid is much higher than that of the imaging. In order to have a more consistent comparison between experiments and simulations, an ensemble average over multiple injections would be preferable. Due to the unavailability of higher image resolution, spatial filtering of the LES CH_2O contours was not carried out in this study. The further upstream appearance of formaldehyde can be attributed to the relatively reactive chemical mechanism used in this study, which is consistent with previous chemical mechanism studies performed by Wehrfritz *et al.* [41]. Additional experimental studies from Maes *et al.* [64] also reported formaldehyde fluorescence signals up to 10 mm axial position downstream of the injector tip - the location of the laser sheet. More importantly, a void region is clearly visible at 0.49 ms for both the simulation and experiment, giving clear indications of second stage ignition. This further shows that the CSE-FGM combustion model is capable of not only capturing ignition delay and flame lift-off length but also describing some underlying physical processes in high pressure diesel fuel spray combustion accurately.

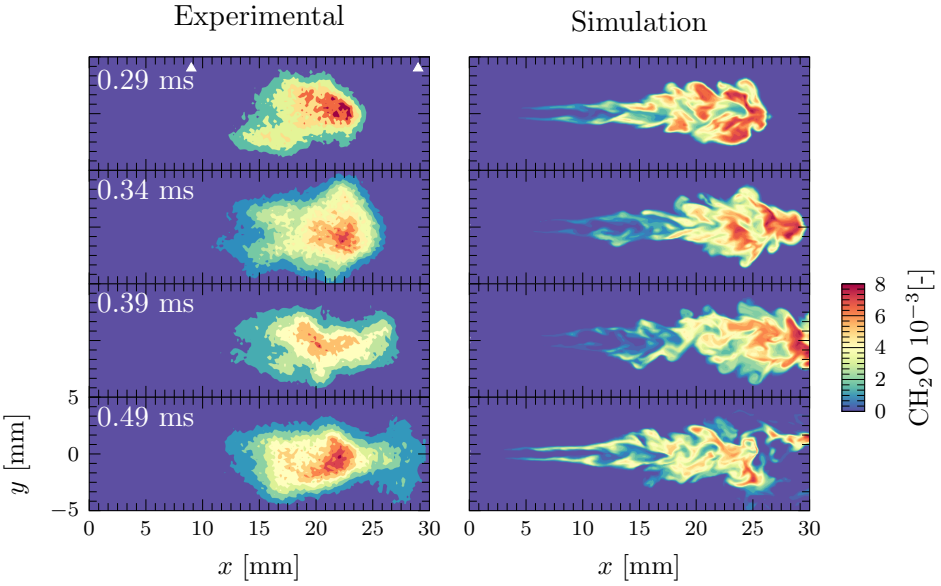

Figure 20. Comparison of single injection false color images of formaldehyde PLIF [63] (left) and single realisation LES (right) spatial formaldehyde distribution for the 900K "Spray A" baseline condition at various timings during ignition. White mark indicates the laser sheet. The colour bar in this figure only applies to the LES simulation as there is no quantitative data from experiments.

6.2. Realisation Variations

Following the study of the transient spray ignition processes, the variation with different LES realisations, the ensemble-average of 5 realisations, and RANS predictions

are presented to qualitatively study the differences between the LES and RANS models, and also to quantify the differences between LES realisations. Figure 21 presents a comparison of mixture fractions and temperature fields between different LES realisations, ensemble-averaged 5 LES realisations, and RANS predictions at 0.7 ms for the 900 K "Spray A" baseline condition. The RANS contour clearly presents a smoother flame structure with axis-symmetric features for both mixture fraction and temperature. The single realisation prediction of LES shows a completely asymmetric structure where substantial fluctuations are present between realisations. The ensemble average of 5 LES realisations shows a much smoother contour like RANS. It is also worth noting that for the ensemble averaged LES simulations, the Z_{st} line crosses closer to the jet centerline, overlapping more of the high temperature region compared to single LES simulation realisation. This is similar to the behaviour of the RANS simulation. However, the distribution of the temperature is still quite different when comparing the ensemble-averaged LES with RANS. Ensemble averaged LES results show a higher temperature region around 40 mm downstream, away from the spray axis, and relatively low-temperature regions around the flame lift-off region and the leading flame region close to the spray axis. The predictions of RANS present similar temperature magnitude along the stoichiometric mixture fraction line. However, jet penetration is different for the RANS and LES predictions, which will have some influence on the flame locations and temperature distributions. The realisation variation was also examined in the mixture fraction space and only a very subtle difference was observed (not shown). Although RANS CSE-FGM is capable of observing global flame characteristics, the mixing field is better resolved with the LES calculations; therefore, predictions are expected to be both quantitatively and qualitatively better than RANS. With this in mind, the further study of the flame stabilization mechanism will be focused on using the CSE/LES simulations.

6.3. Flame Stabilisation

The presence of rapid convection and diffusion in a transient diesel spray flame has raised various questions about the flame stabilization mechanisms. Figure 22 highlights the main characteristics of a typical stabilized spray flame and their visual definition. Numerical simulations and experimental data have suggested autoignition events upstream of (or near) the lift-off length play a significant role in flame stabilization [65][66][46][67]. Therefore, it is critical to have an accurate prediction of flame lift-off length, and hence to capture the underlying flame stabilization mechanism. As mentioned before, experimental flame lift-off length is given by the OH^* chemiluminescence [66]; in contrast, the CFD flame lift-off is provided by the OH concentration. More recently, Maes *et al.* [64] performed experimental measurements using planar laser-induced fluorescence (PLIF) of ground state OH at various ECN "Spray A" conditions given the opportunity for direct qualitative comparison between experimental and simulation lift-off length. For the experimental study, ensemble averaged images of 5-20 injections, depending on the test condition, were obtained. Figure 23 compares the simulated ground state OH mass fraction with the measured ensemble averaged OH-PLIF results. The white arrows in the figure indicate the approximate limits of the laser sheet. It is worth noting that the less bright OH branch on the right of the experimental data is attributed to the attenuation of the excitation laser light by the spray. The simulation captures the OH field qualitatively, as demonstrated by the two distinct branches of OH where each branch expands in the radial direction as

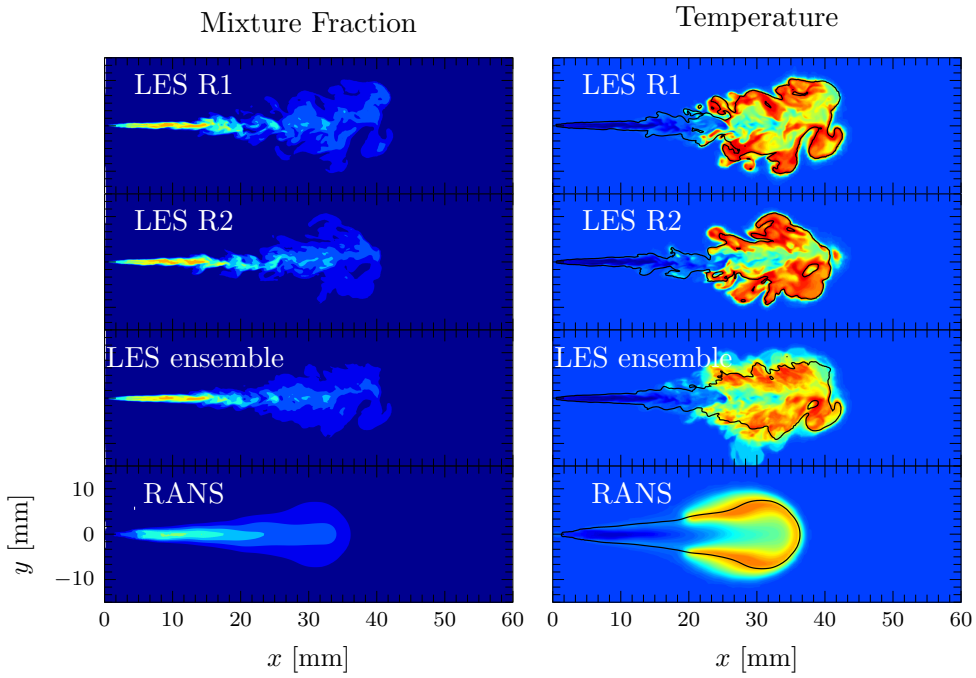

Figure 21. Realization variation, ensemble average of 5 LES calculations and RANS results of mixture fraction field (left) and temperature field (right) at 0.7ms for the 900K "Spray A " baseline condition. The black line is the stoichiometric mixture fraction contour

the axial distance is increased. In addition, the onset of OH is comparable between simulation and experiment at approximately $x = 15$ mm. However, the simulation predicts higher concentrations of OH further downstream compared to the experiment. This is possibly due to the experimental measurement technique as the laser sheet intensity distribution used in the experiment is known to bias the represented signal at near lift-off location.

As mentioned before, the LES simulations suggested a quasi-steady state flame is established around 0.7 ms ASI, which is consistent with the experiment where more coherent images are observed after 0.7 ms [64]. Therefore, for the comparison of quasi-steady state flame structure, the OH distribution at 1.2 ms ASI is compared to the 4.7 ms OH PLIF measurements in Figure 24. The simulation is again qualitatively comparable to the experiment with two branches expanding in both radial and axial directions. However, the onset location of OH is underpredicted at this time; also, the OH field is more diffuse than the separate OH branches seen in the experiment. This could be attributed to the experimental methodology, where it can be seen from [64] that differences in optical setup resulted in qualitatively different OH distributions at the same test condition. These differences are shown in Figure 25, where the OH structure as measured by IFP Energies nouvelles (IFPEn) is considerably more diffuse than that of Eindhoven University of Technology (TU/e). In general, the typically observed spray structure has a fuel rich core enveloped by a high temperature field as indicated by the presence of OH. The onset presence of OH (18.94 mm) is also reported in the experiment approximately to be 1.55 mm downstream of the onset OH^* (17.39 mm). This is an important consideration as it will influence confidence in the CFD flame lift-off length: the threshold may not be a sufficiently suitable criteria to make absolute comparisons against experimental measurements based on OH.

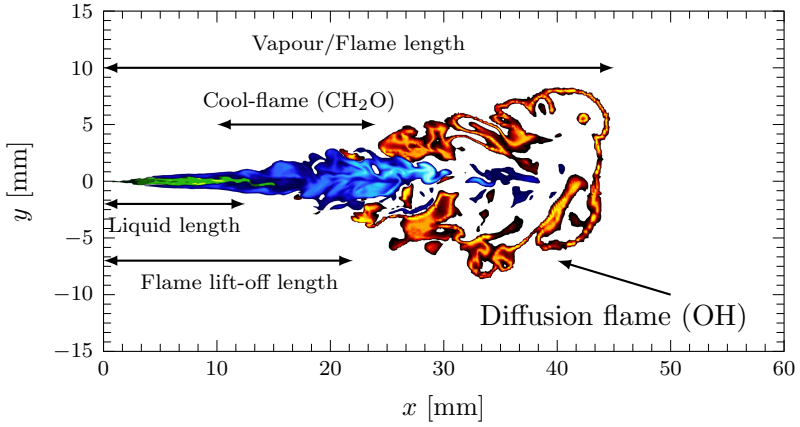

Figure 22. Schematic of a stabilized spray flame: green is the n-dodecane fuel, blue is the cool-flame and is defined by the presence of formaldehyde and orange is the high temperature diffusion flame which is defined by the presence of hydroxyl.

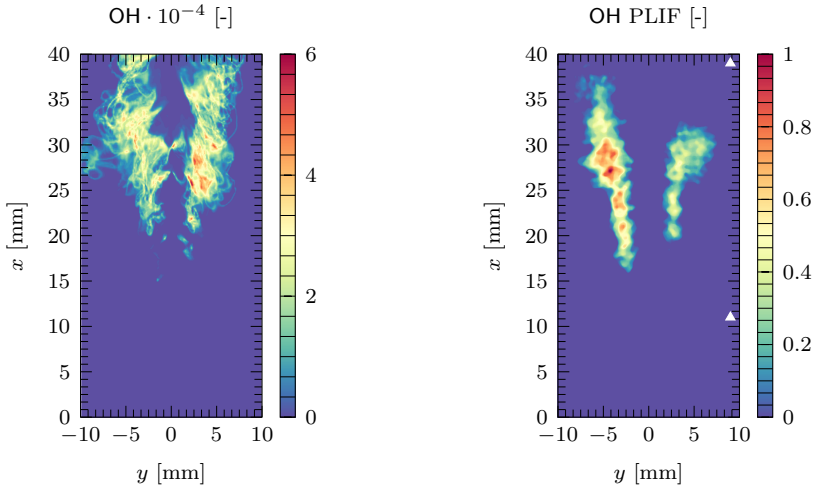

Figure 23. Comparison of (a) CSE-FGM/LES spatially averaged OH mass fraction and (b) ensemble-averaged experimental PLIF OH measurements at 0.8 ms ASI. Laser sheet location is marked by white triangles. Experimental data repeated from [64].

Previously, Pei *et al.* investigated the effect of implied convection, diffusion, and reaction terms on stabilisation mechanisms [46]. The study suggested the diesel spray stabilisation mechanism can be perceived as autoignition controlled but modulated by flame propagation. This indicates flame lift-off length is regulated by the axial distance at which flow conditions do not support the formation and growth of ignition kernels. Scalar dissipation rate measures the mixing rate of fuel and oxidizer, which significantly impacts the flow field, and therefore has a strong influence on the autoignition and flame structure. The filtered scalar dissipation rate $\tilde{\chi}$ in LES can be decomposed into resolved ($\tilde{\chi}_r$) and the subgrid part ($\tilde{\chi}_{sgs}$) is given by Tillou *et al.* [68]:

$$\tilde{\chi} = \tilde{\chi}_{sgs} + \tilde{\chi}_r = 2D|\frac{\partial \tilde{Z}}{\partial x}|^2 + \frac{D_t}{\Delta^2}\widetilde{Z''^2} \tag{23}$$

Here D is the molecular diffusivity of the mixture, D_t is the turbulent diffusivity, and

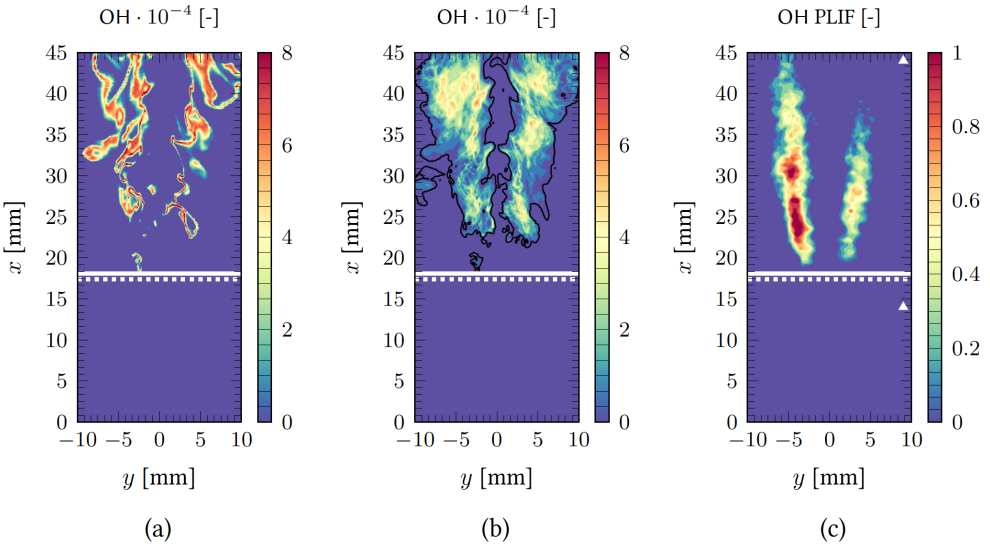

Figure 24. Comparison of (a) CSE-FGM/LES instantaneous OH mass fraction field at 1.20 ms ASI, (b) spatially-averaged CSE-FGM/LES OH mass fraction field at 1.20 ms ASI, (c) ensemble-averaged OH PLIF measurements at 4.70 ms ASI. The solid white line denotes CSE-FGM/LES flame lift-off value; the white dashed line denotes steady state experimental flame lift-off value (based on OH) from Maes *et al.* [64]. Laser sheet location marked by white triangles. Experimental images reproduced from [64]

Δ is the grid size. The process of flame stabilisation can be visualised by tracking an ignition kernel near the flame lift-off length. Figure 27 focuses on the temperature and scalar dissipation rate evolution near the flame lift-off location for the CSE-FGM/LES model at quasi-steady state (around 1 ms ASI). Large fluctuations in the scalar field indicate the highly unsteady nature of the diesel spray jet. Low and high scalar dissipation rates are seen to be interwoven within the flame structure. At 0.95 ms, there is an ignition spot upstream of the flame (marked by (i)). Top right of Figure 26 provides the radial profiles of temperature and scalar dissipation rate at this location. This indicates that the ignition is indeed occurring in regions of low scalar dissipation rate. Further tracking of the ignition spot from 0.95 ms to 0.99 ms shows its expansion and connection to the main flame. Bottom right of Figure 26 provides the radial profiles of temperature and scalar dissipation rate at the same location for 0.97 ms (marked by (ii)), where low dissipation rate is observed near the region of the ignition spot. Following the initial ignition, convection drives these hot regions further downstream, merging with other gas pockets and finally the main flame (iv) at 1.02 ms ASI. In addition to ignition taking place, extinction also occurs in this flame. This is observed by tracking an ignited gas pocket denoted by sub-label (A) at 0.95 ms ASI in Figure 27. The radial profiles of temperature and scalar dissipation at this point show similar behaviour to that seen in top left of Figure 26 . However, at 0.97 ms ASI, convection of the vapour jet upstream leads to large scalar gradients in the region around point (A) and local extinction of the flame occurs as highlighted by (B). The observation obtained here suggests that diesel spray flame stabilisation may be controlled by autoignition.

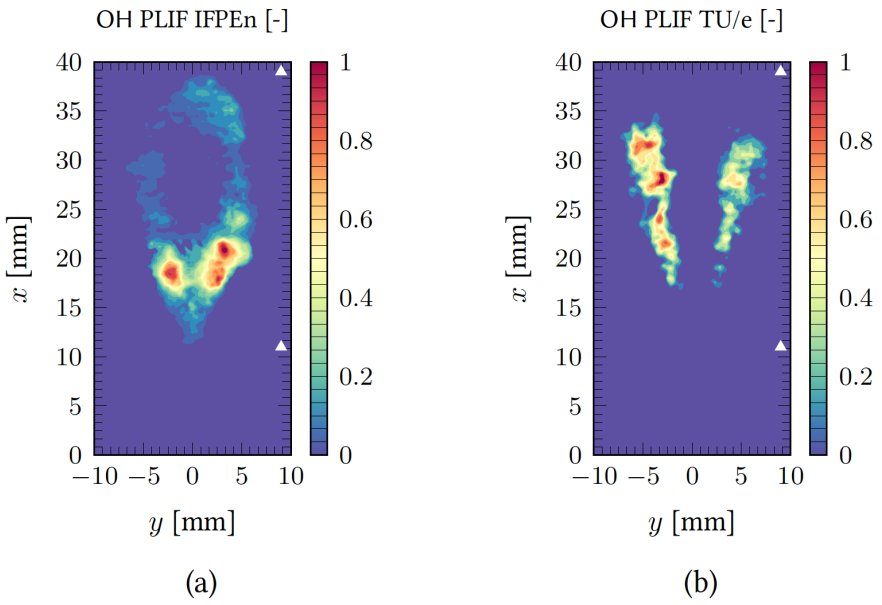

Figure 25. Comparison of ensemble-averaged experimental PLIF OH measurements at 0.7 ms ASI for (a) IFPEn and (b) TU/e. Laser sheet location is marked by white triangles. Experimental images reproduced from [64].

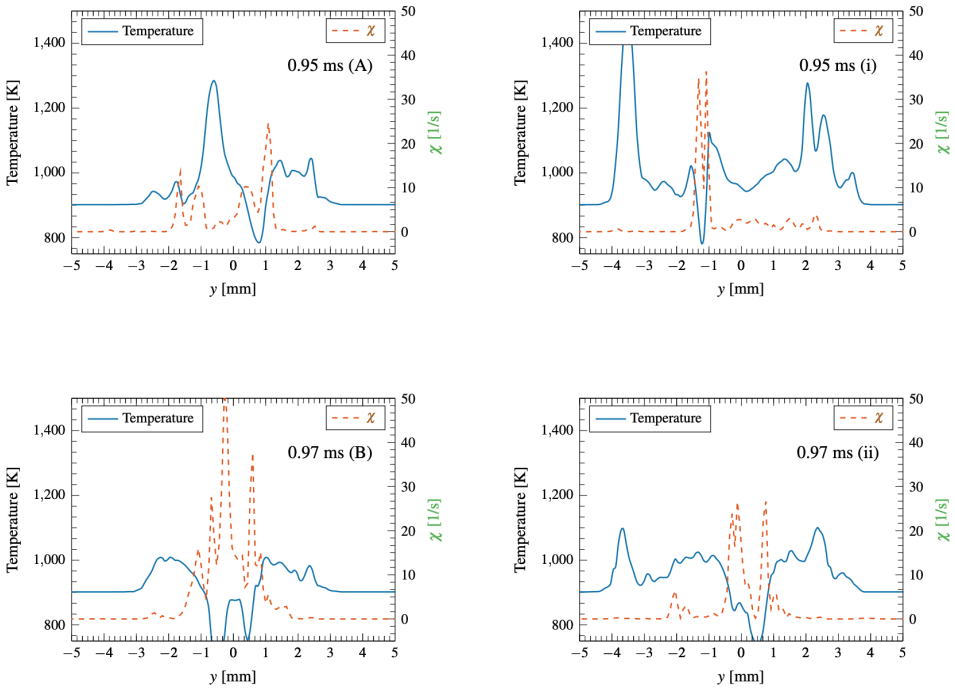

Figure 26. Temperature and scalar dissipation rate comparison at different axial locations: Top: radial scalar dissipation at 0.95 ms ASI at point (A) and point (i) in Figure 27, Bottom: radial scalar dissipation at 0.97 ms ASI at point (B) and point (ii) in Figure 27

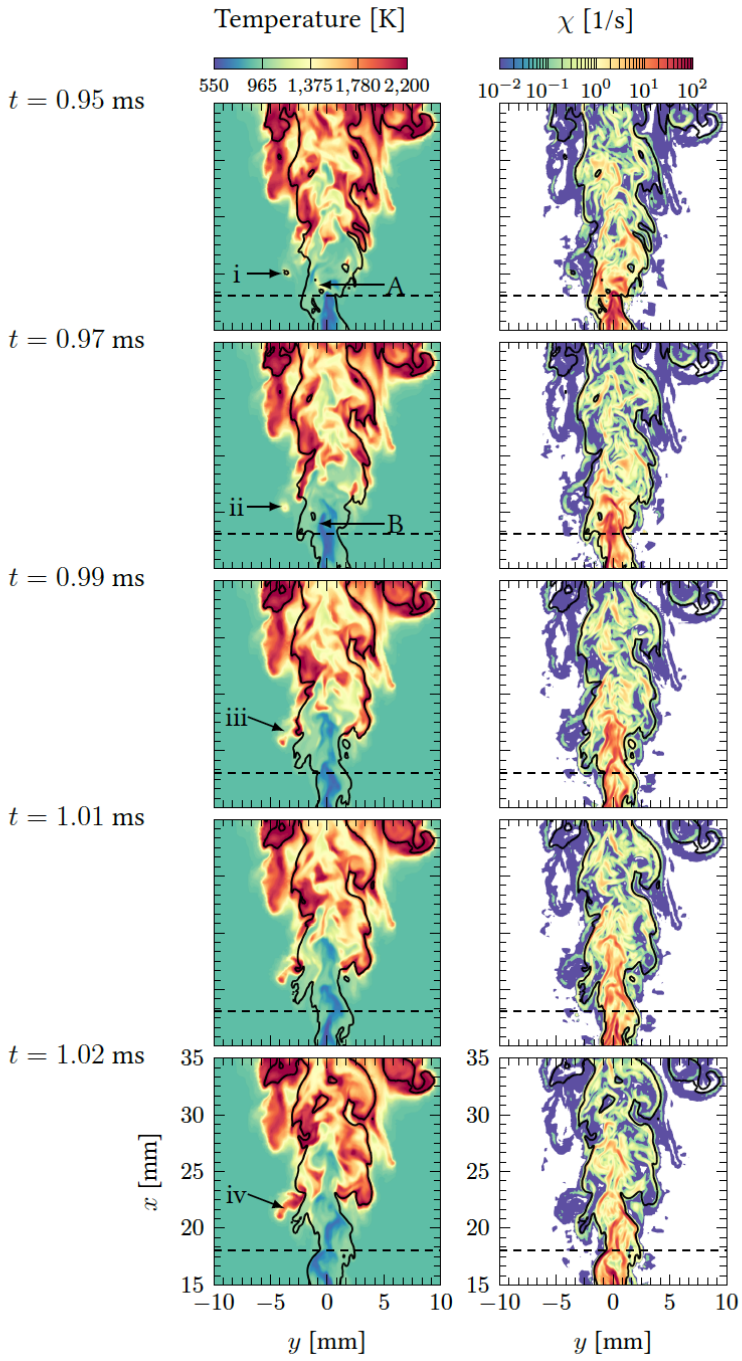

Figure 27. Temperature (left) and scalar dissipation (right) evolution near the flame lift-off length. The black dashed line marks the simulations flame lift-off length. The solid black line is the contour of stoichiometric mixture fraction.

7. Conclusions

In this study, a novel combustion modelling approach (CSE-FGM) was presented and validated against spray flame experiments with both the RANS and LES frameworks. The approach combines the conditional moment hypothesis with tabulated chemistry given by the unsteady flamelet generated manifold. This approach enables the combustion model - Conditional Source-term Estimation to be extended to a more complicated fuel. Extensive validation of the CSE-FGM was carried out for the 900 K ECN "Spray A" conditions with a 54 species, 268 reactions, n-dodecane chemical mechanism covering the low temperature combustion region for the diesel fuel surrogate. The findings are summarized in as follows:

- The CSE-FGM based combustion modelling approach has successfully demonstrated the capability of realistically predicting the essential structure of the diesel-fueled transient spray combustion processes. The unique structure of the spray jet flame consisting of a liquid fuel jet, a low temperature oxidation zone, and a high temperature oxidation zone is well captured.
- Both RANS and LES paradigms are capable of quantitatively predicting the autoignition time and flame lift-off length with slight overprediction in the RANS simulations.
- The LES simulation suggest two stage ignition is indeed captured by the CSE-FGM combustion model. In LES, multiple ignition kernels were found in the mixing layer where only one location was seen in the RANS predictions. The LES temperature field showed reasonably good agreement with the experimental schlieren images in terms of the location and rate of flame propagation.
- The comparison of the simulated formaldehyde field with experiments showed that the major formaldehyde appearance prior to ignition is observed at the tip of the fuel-rich gas jet. Second stage ignition is well captured by the consumption of formaldehyde near the time of autoignition.
- Analysis of the flame stabilization mechanism showed good agreement for the OH field compared to experiments. Both autoignition and local extinction were found near the flame lift-off length which suggests the flame stabilization is controlled by autoignition but modulated by flame propagation

From a combustion modelling viewpoint, the CSE-FGM model has been shown to be well suited for detailed combustion analysis of diesel spray flames within both RANS and LES frameworks. We note that the model might be further refined by the incorporaton of a second conditioning variable or the inclusion of differential diffusion.

References

[1] Y. Wright, G.D. Paola, K. Boulouchos, and E. Mastorakos, *Simulations of spray autoignition and flame establishment with two-dimensional cmc*, Combustion and Flame 143 (2005), pp. 402 – 419.

[2] P. Domingo, L. Vervisch, and D. Veynante, *Large-eddy simulation of a lifted methane jet flame in a vitiated coflow*, Combustion and Flame 152 (2008), pp. 415 – 432.

[3] C. Bekdemir, E. Rijk, L. Somers, P. Goey, and B. Albrecht, *On the application of the flamelet generated manifold (fgm) approach to the simulation of an igniting diesel spray* (2010).

[4] J.V. Oijen and L.D. Goey, *Modelling of premixed laminar flames using flamelet-generated manifolds*, Combustion Science and Technology 161 (2000), pp. 113–137.
[5] A.Y. Klimenko, *Multicomponent diffusion of various admixtures in turbulent flow*, Fluid Dynamics 25 (1990), pp. 327–334.
[6] R.W. Bilger, *Conditional moment closure for turbulent reacting flow*, Physics of Fluids A: Fluid Dynamics 5 (1993), pp. 436–444.
[7] A. Masri, R. Dibble, and R. Barlow, *The structure of turbulent nonpremixed flames of methanol over a range of mixing rates*, Combustion and Flame 89 (1992), pp. 167 – 185.
[8] J.H. Frank, S.A. Kaiser, and M.B. Long, *Reaction-rate, mixture-fraction, and temperature imaging in turbulent methane/air jet flames*, Proceedings of the Combustion Institute 29 (2002), pp. 2687–2694.
[9] S. Patwardhan, S. De, K. Lakshmisha, and B. Raghunandan, *CMC simulations of lifted turbulent jet flame in a vitiated coflow*, Proceedings of the Combustion Institute 32 (2009), pp. 1705 – 1712.
[10] A.E. Sayed and C.B. Devaud, *Conditional Moment Closure (CMC) applied to autoignition of high pressure methane jets in a shock tube*, Combustion Theory and Modelling 12 (2008), pp. 943–972.
[11] M. Fairweather and R. Woolley, *First- and second-order elliptic conditional moment closure calculations of piloted methane diffusion flames*, Combustion and Flame 150 (2007), pp. 92 – 107.
[12] A. Kronenburg, R. Bilger, and J. Kent, *Modeling soot formation in turbulent methane–air jet diffusion flames*, Combustion and Flame 121 (2000), pp. 24 – 40.
[13] Y.M. Wright, M. Bolla, K. Boulouchos, G. Borghesi, and E. Mastorakos, *Conditional moment closure for two-phase flows – a review of recent developments and application to various spray combustion configurations*, AIP Conference Proceedings 1642 (2015), pp. 433–440.
[14] Y.M. Wright, O. Margari, K. Boulouchos, G. De Paola, and E. Mastorakos, *Experiments and simulations of n-heptane spray auto-ignition in a closed combustion chamber at diesel engine conditions*, Flow, Turbulence and Combustion 84 (2010), pp. 49–78.
[15] G. Borghesi, E. Mastorakos, C.B. Devaud, and R.W. Bilger, *Modeling evaporation effects in conditional moment closure for spray autoignition*, Combustion Theory and Modelling 15 (2011), pp. 725–752.
[16] S. C. Blomberg L. Zeugin and M. Bolla., *Modeling Split Injections of ECN "Spray A" Using a Conditional Moment Closure Combustion Model with RANS and LES*, SAE Int. J. Engines 9 (2016).
[17] A. Klimenko and R. Bilger, *Conditional moment closure for turbulent combustion*, Progress in Energy and Combustion Science 25 (1999).
[18] K. Han and K.Y. Huh, *First and second order lagrangian conditional moment closure method in turbulent nonpremixed flames*, Proceedings of the Combustion Institute 35 (2015).
[19] H.K. Seung, Y.H. Kang, and W.B. Robert, *Second-order conditional moment closure modeling of local extinction and reignition in turbulent non-premixed hydrocarbon flames*, Proceedings of the Combustion Institute 29 (2002), pp. 2131 – 2137.
[20] C.M. Cha, G. Kosaly, and H. Pitsch, *Modeling extinction and reignition in turbulent nonpremixed combustion using a doubly-conditional moment closure approach*, Physics of Fluids 13 (2001).
[21] N. Peters, *Laminar diffusion flamelet models in non-premixed turbulent combustion*, Progress in Energy and Combustion Science 10 (1984), pp. 319 – 339.
[22] A. Kronenburg, *Double conditioning of reactive scalar transport equations in turbulent nonpremixed flames*, Physics of Fluids 16 (2004), pp. 2640–2648.
[23] W.K. Bushe and H. Steiner, *Conditional moment closure for large eddy simulation of nonpremixed turbulent reacting flows*, Physics of Fluids 11 (1999), pp. 1896–1906.
[24] J. Labahn and C. Devaud, *Investigation of conditional source-term estimation applied to a non-premixed turbulent flame*, Combustion Theory and Modelling 17 (2013), pp. 960–982.

[25] R.W. Grout, W.K. Bushe, and C. Blair, *Predicting the ignition delay of turbulent methane jets using conditional source-term estimation*, Combustion Theory and Modelling 11 (2007), pp. 1009–1028.

[26] L.J.W. Dovizio D. and D.C. B., *Doubly Conditional Source-term Estimation (DCSE) applied to a series of lifted turbulent jet flames in cold air*, Combustion and Flame 162 (2015).

[27] L. Nicholson, X. Fang, J. Camm, M. Davy, and D. Richardson, *Comparison of Transient Diesel Spray Break-Up Between Two Computational Fluid Dynamics Codes*, in *WCX World Congress Experience*, apr. SAE International, 2018.

[28] X. Fang, R. Ismail, M. H. Davy, and J. Camm, *Numerical studies of combustion recession on ECN diesel Spray A*, ASME. Internal Combustion Engine Division Fall Technical Conference (2018-9597).

[29] S.S. Girimaji, *Assumed β-pdf model for turbulent mixing: Validation and extension to multiple scalar mixing*, Combustion Science and Technology 78 (1991), pp. 177–196.

[30] H.J. Wang M. and W.K. Bushe, *Simulation of a turbulent non-premixed flame using conditional source-term estimation with trajectory generated low-dimensional manifold*, Proceedings of the Combustion Institute 31 (2007), pp. 1701 – 1709.

[31] W. L. Jeffrey, B. D. Cecile, A. S. Timothy, and Kyle J. Daun, *Inverse analysis and regularisation in conditional source-term estimation modelling*, Combustion Theory and Modelling 18 (2014), pp. 474–499.

[32] H.P. Tsui and W.K. Bushe, *Conditional source-term estimation using dynamic ensemble selection and parallel iterative solution*, Combustion Theory and Modelling 20 (2016), pp. 812–833.

[33] P.C. Hansen, *Numerical tools for analysis and solution of fredholm integral equations of the first kind*, Inverse Problems 8 (1992), p. 849.

[34] Dovizio, D. and Devaud, C.B., *Doubly Conditional Source-term Estimation (DCSE) for the modelling of turbulent stratified V-shaped flame*, Combustion and Flame 172 (2016).

[35] H. Steiner and W.K. Bushe, *Large eddy simulation of a turbulent reacting jet with conditional source-term estimation*, Physics of Fluids 13 (2001), pp. 754–769.

[36] U. Maas and S.B. Pope, *Simplifying chemical kinetics: Trajectory generated low-dimensional manifolds*, Mechanical and Aerospace Engineering Report: FDA 93-11 .

[37] M. Wang, J. Huang, and W.K. Bushe, *Simulation of a turbulent non-premixed flame using conditional source-term estimation with trajectory generated low-dimensional manifold*, Proceedings of the Combustion Institute 31 (2007), pp. 1701 – 1709.

[38] S. Asenbauer, *Examining spray models for conditional source-term estimation combustion simulation*, Ph.D. diss., 2015.

[39] G. Stahl and J. Warnatz, *Numerical investigation of time-dependent properties and extinction of strained methane and propane-air flamelets*, Combustion and Flame 85 (1991), pp. 285–299.

[40] Chem1D, *one-dimensional laminar flame code, eindhoven university of technology*, URL http://www. combustion. tue. nl/chem1d .

[41] A. Wehrfritz, O. Kaario, V. Vuorinen, and B. Somers, *Large eddy simulation of n-dodecane spray flames using flamelet generated manifolds*, Combustion and Flame 167 (2016), pp. 113 – 131.

[42] R. Bilger, S. Starner, and R. Kee, *On reduced mechanisms for methane air combustion in nonpremixed flames*, Combustion and Flame 80 (1990), pp. 135 – 149.

[43] U. Egüz, S. Ayyapureddi, C. Bekdemir, B. Somers, and P. de Goey, *Manifold resolution study of the FGM method for an igniting diesel spray*, Fuel 113 (2013), pp. 228–238.

[44] A. Yoshizawa and K. Horiuti, *A statistically-derived subgrid-scale kinetic energy model for the large-eddy simulation of turbulent flows*, Journal of the Physical Society of Japan 54 (1985), pp. 2834–2839.

[45] S. Menon, P.K. Yeung, and W.W. Kim, *Effect of subgrid models on the computed interscale energy transfer in isotropic turbulence*, Computers & Fluids 25 (1996), pp. 165 – 180.

[46] Y. Pei, S. Som, E. Pomraning, P.K. Senecal, S.A. Skeen, J. Manin, and L.M. Pickett, *Large*

eddy simulation of a reacting spray flame with multiple realizations under compression ignition engine conditions, Combustion and Flame 162 (2015), pp. 4442 – 4455.

[47] L. Pickett and G. Bruneaux, *Engine combustion network. combustion research facility, sandia national laboratories, livermore, ca*, See http://www. sandia. gov/ECN (2018).

[48] Q. Xue, W. Som, P. Senecal, and E. Pomraning, *A Study of Grid Resolution and SGS Models for LES Under Non-Reacting Spray Conditions*, in *25th Annual Conference on Liquid Atomization and Spray Systems, Pittsburgh, PA*. 2013.

[49] X. Fang, R. Ismail, and M. Davy, *A Study on Kinetic Mechanisms of Diesel Fuel Surrogate n-Dodecane for the Simulation of Combustion Recession*, in *SAE Technical Paper*, 04. SAE International, 2019.

[50] P. Senecal, E. Pomraning, Q. Xue, S. Som, S. Banerjee, B. Hu, K. Liu, and J. Deur, *Large eddy simulation of vaporizing sprays considering multi-injection averaging and grid-convergent mesh resolution*, Journal of Engineering for Gas Turbines and Power 136 (2014), p. 111504.

[51] M.M. Ameen, Y. Pei, and S. Som, *Computing Statistical Averages from Large Eddy Simulation of Spray Flames*, in *SAE 2016 World Congress and Exhibition*. SAE International 2016-01-0585, 2016.

[52] L.M. Pickett, J. Manin, C.L. Genzale, D.L. Siebers, M.P.B. Musculus, and C.A. Idicheria, *Relationship between diesel fuel spray vapor penetration/dispersion and local fuel mixture fraction*, SAE Int. J. Engines 4 (2011), pp. 764–799.

[53] M. Meijer and L. Somers, *Engine Combustion Network: "Spray A" basic measurements and advanced diagnostics*, in *Proceedings of the 12th International Conference on Liquid Atomization and Spray Systems, ICLASS 2012, 2-6 September 2012, Heidelberg, Germany*. 2012.

[54] T. Yao, Y. Pei, B. Zhong, S. Som, and T. Lu, *A hybrid mechanism for n-dodecane combustion with optimized low-temperature chemistry* (2015).

[55] S. Vasu, D. Davidson, Z. Hong, V. Vasudevan, and R. Hanson, *n-dodecane oxidation at high-pressures: Measurements of ignition delay times and oh concentration time-histories*, Proceedings of the Combustion Institute 32 (2009), pp. 173 – 180.

[56] T. Yao, Y. Pei, B.J. Zhong, S. Som, T. Lu, and K.H. Luo, *A compact skeletal mechanism for n-dodecane with optimized semi-global low-temperature chemistry for diesel engine simulations*, Fuel 191 (2017), pp. 339 – 349.

[57] P. Kundu, M.M. Ameen, and S. Som, *Importance of turbulence-chemistry interactions at low temperature engine conditions*, Combustion and Flame 183 (2017), pp. 283 – 298.

[58] R.N. Dahms, G.A. Paczko, S.A. Skeen, and L.M. Pickett, *Understanding the ignition mechanism of high-pressure spray flames*, Proceedings of the Combustion Institute 36 (2017), pp. 2615 – 2623.

[59] P. Zhao and C.K. Law, *The role of global and detailed kinetics in the first-stage ignition delay in ntc-affected phenomena*, Combustion and Flame 160 (2013), pp. 2352 – 2358.

[60] E. Mastorakos, *Ignition of turbulent non-premixed flames*, Progress in Energy and Combustion Science 35 (2009), pp. 57 – 97.

[61] L.M. Pickett, *Introducing the engine combustion network*, in *International Multidimensional Engine Modeling Users Group Meeting*. 2008.

[62] L.M. Pickett, C.L. Genzale, G. Bruneaux, L.M. Malbec, L. Hermant, C. Christiansen, and J. Schramm, *Comparison of diesel spray combustion in different high-temperature, high-pressure facilities*, SAE Int. J. Engines 3 (2010), pp. 156–181.

[63] S.A. Skeen, J. Manin, and L.M. Pickett, *Simultaneous formaldehyde PLIF and high-speed schlieren imaging for ignition visualization in high-pressure spray flames*, Proceedings of the Combustion Institute 35 (2015), pp. 3167 – 3174.

[64] N. Maes, M. Meijer, N. Dam, B. Somers, H.B. Toda, G. Bruneaux, S.A. Skeen, L.M. Pickett, and J. Manin, *Characterization of spray a flame structure for parametric variations in ecn constant-volume vessels using chemiluminescence and laser-induced fluorescence*, Combustion and Flame 174 (2016), pp. 138 – 151.

[65] S. Skeen, J. Manin, and L. Pickett, *Visualization of Ignition Processes in High-Pressure*

Sprays with Multiple Injections of n-Dodecane, SAE Int. J. Engines 8 (2015).

[66] L.M. Pickett, S. Kook, H. Persson, and Öivind Andersson, *Diesel fuel jet lift-off stabilization in the presence of laser-induced plasma ignition*, Proceedings of the Combustion Institute 32 (2009), pp. 2793 – 2800.

[67] S. Navarro-Martinez and A. Kronenburg, *Flame stabilization mechanisms in lifted flames*, Flow, Turbulence and Combustion 87 (2011), pp. 377–406.

[68] J. Tillou, J.B. Michel, C. Angelberger, and D. Veynante, *Assessing les models based on tabulated chemistry for the simulation of diesel spray combustion*, Combustion and Flame 161 (2014), pp. 525 – 540.